RESEARCH ARTICLE

Subversion of Serotonin Receptor Signaling in Osteoblasts by Kynurenine Drives Acute Myeloid Leukemia

Marta Galán-Díez[1], Florence Borot[2], Abdullah Mahmood Ali[2,3], Junfei Zhao[4], Eva Gil-Iturbe[5], Xiaochuan Shan[6], Na Luo[1], Yongfeng Liu[7], Xi-Ping Huang[7], Brygida Bisikirska[1], Rossella Labella[1], Irwin Kurland[8], Bryan L. Roth[7,9], Matthias Quick[5,10], Siddhartha Mukherjee[2,3,11], Raul Rabadán[4,12], Martin Carroll[6], Azra Raza[2,3,11], and Stavroula Kousteni[1,2,11,13]

Illustration by Bianca Dunn

ABSTRACT Remodeling of the microenvironment by tumor cells can activate pathways that favor cancer growth. Molecular delineation and targeting of such malignant-cell nonautonomous pathways may help overcome resistance to targeted therapies. Herein we leverage genetic mouse models, patient-derived xenografts, and patient samples to show that acute myeloid leukemia (AML) exploits peripheral serotonin signaling to remodel the endosteal niche to its advantage. AML progression requires the presence of serotonin receptor 1B (HTR1B) in osteoblasts and is driven by AML-secreted kynurenine, which acts as an oncometabolite and HTR1B ligand. AML cells utilize kynurenine to induce a proinflammatory state in osteoblasts that, through the acute-phase protein serum amyloid A (SAA), acts in a positive feedback loop on leukemia cells by increasing expression of IDO1—the rate-limiting enzyme for kynurenine synthesis—thereby enabling AML progression. This leukemia–osteoblast cross-talk, conferred by the kynurenine–HTR1B–SAA–IDO1 axis, could be exploited as a niche-focused therapeutic approach against AML, opening new avenues for cancer treatment.

SIGNIFICANCE: AML remains recalcitrant to treatments due to the emergence of resistant clones. We show a leukemia-cell nonautonomous progression mechanism that involves activation of a kynurenine–HTR1B–SAA–IDO1 axis between AML cells and osteoblasts. Targeting the niche by interrupting this axis can be pharmacologically harnessed to hamper AML progression and overcome therapy resistance.

INTRODUCTION

Hematologic malignancies have long been thought to be exclusively driven by genetic or epigenetic mutations within hematopoietic cells. Besides these classic mechanisms, demonstrated in animal models and human cells, there is increasing evidence that the bone marrow (BM) microenvironment or niche plays a role in the pathogenesis, maintenance, and resistance to treatment of malignant clones (1–5). Accordingly, the niche can enable immune evasion and activation of survival and differentiation pathways favoring malignant-cell maintenance, defense against oxidative stress, and protection from chemotherapy.

Acute myeloid leukemia (AML), a heterogeneous clonal hematopoietic neoplasm and one of the most common hematologic malignancies of the elderly (6, 7), remains recalcitrant to targeted therapies due to the emergence of preexistent or *de novo* therapy-resistant leukemic clones. Against this backdrop, cell nonautonomous contributions of the niche to disease development, propagation, and maintenance (8, 9) may hold promise for the development of new treatment approaches that focus on the niche that sustains AML. Particularly among niches, alterations in the osteoblastic compartment lead to myelodysplastic syndrome (MDS) and AML in mice (10–15) and are associated with myeloproliferative neoplasms, MDS, and AML in patients (16, 17). In addition, osteoblasts can exert a tumor-suppressor role in myeloid disorders (18–20) or can be remodeled by dysplastic cells to reinforce leukemia (17, 21–23). Osteoblast numbers are decreased in patients with MDS and AML, and their ablation increases leukemia burden, whereas maintaining the osteoblastic pool reduces tumor burden and prolongs survival (19). However, the mechanisms that mediate the leukemia cell–osteoblast communication, the molecular events that affect leukemia outcome, and whether this cross-talk could be harnessed for a therapeutic purpose remain largely unexplored.

In addressing these questions, herein we show that AML cells exploit serotonin receptor 1B (*HTR1B*) signaling in osteoblasts to proliferate. Remarkably, this proliferative pathway is not driven by serotonin [5-hydroxytryptamine (5-HT)] but by another tryptophan (Trp) catabolite, kynurenine (Kyn), which acts as a new ligand of HTR1B in a function distinct from its reported immunoregulatory properties. Using AML mouse models, patient-derived xenografts (PDX), as well as samples from patients with AML and MDS, we observed that AML cells utilize Kyn to remodel the BM niche and amplify their growth by inducing a proinflammatory signature in

[1]Department of Physiology and Cellular Biophysics, Columbia University, New York, New York. [2]Herbert Irving Comprehensive Cancer Center (HICCC), Columbia University, New York, New York. [3]Myelodysplastic Syndromes Center, Columbia University, New York, New York. [4]Program for Mathematical Genomics, Department of Systems Biology, Columbia University, New York, New York. [5]Department of Psychiatry, Columbia University, New York, New York. [6]Department of Medicine, University of Pennsylvania, Philadelphia, Pennsylvania. [7]NIMH Psychoactive Drug Screening Program, Department of Pharmacology, University of North Carolina Chapel Hill Medical School, Chapel Hill, North Carolina. [8]Department of Medicine, Albert Einstein College of Medicine, Bronx, New York. [9]Division of Chemical Biology and Medicinal Chemistry, Eshelman School of Pharmacy, University of North Carolina at Chapel Hill, Chapel Hill, North Carolina. [10]Division of Molecular Therapeutics, New York State Psychiatric Institute, New York, New York. [11]Edward P. Evans Center for Myelodysplastic Syndromes at Columbia University, New York, New York. [12]Department of Biomedical Informatics, Columbia University, New York, New York. [13]Columbia Stem Cell Initiative, Columbia University, New York, New York.

Note: Supplementary data for this article are available at Cancer Discovery Online (http://cancerdiscovery.aacrjournals.org/).

Corresponding Authors: Stavroula Kousteni, Phone: 212-305-2068; E-mail: sk2836@cumc.columbia.edu; and Marta Galán-Díez, Department of Physiology and Cellular Biophysics, Columbia University, 650 W. 168th Street, New York, NY 10032. Phone: 212-305-2481; E-mail: martagalandiez@gmail.com

Cancer Discov 2022;12:1106–27

doi: 10.1158/2159-8290.CD-21-0692

osteoblasts. Among several upregulated proinflammatory molecules, the acute-phase protein serum amyloid A (SAA) is the signal emitted by osteoblasts that instructs AML cells to stimulate upregulation of indoleamine 2,3-dioxygenase-1 (IDO1; the rate-limiting enzyme for Kyn synthesis), selectively promoting AML proliferation. Genetic and pharmacologic inhibition of the Kyn–HTR1B interaction between leukemia cells and osteoblasts hampers AML proliferation. These findings identify a mechanism underlying AML progression that relies on an osteoblast–leukemia cross-talk; as a result, they suggest that a therapy targeting the BM stromal microenvironment—not the clonally expanding AML cells—may be harnessed to manage myeloid malignancies.

RESULTS

Osteoblasts Inhibit AML by a Mechanism Involving Serotonin Signaling

We have previously shown that the maintenance of osteoblast numbers by inhibiting antiproliferative actions of gut-derived serotonin reduces leukemia burden and prolongs survival (19). In this study, we examined whether any means of preserving the osteoblast pool during AML development would suffice to affect disease progression. Osteoblast numbers were maintained by treating leukemic mice with a regimen of intermittent parathyroid hormone (PTH), which increases osteoblast numbers (24, 25) without affecting serotonin signaling. To preserve the integrity of the BM microenvironment and the hematopoietic system, dsRed-MLL/AF9–induced blasts (26–28) from leukemic mice were injected into nonirradiated wild-type (WT) recipient mice (Supplementary Fig. S1A). PTH failed to curtail leukemia growth, as neither disease progression (Supplementary Fig. S1B) nor life span (Fig. 1A) was affected in PTH-treated versus vehicle-treated mice. Moreover, PTH did not affect serotonin signaling because expression of Cyclins D1, D2, and E1 (targets suppressed by serotonin–HTR1B signaling; ref. 29) did not change in the bones of PTH-treated versus vehicle-treated mice (Supplementary Fig. S1C). These results suggested that engagement of a specific pathway dependent on serotonin receptor signaling may mediate the protective effect of osteoblasts against AML progression.

Ablation of *Htr1b* in Osteoblasts Prevents AML Progression

As our results suggest that the protective effect of osteoblasts against leukemia progression does not rely solely on the number of osteoblasts but rather on the engagement of serotonin receptor signaling, we set out to dissect the specific signaling pathway involved. Among the 14 described serotonin receptors, only three are expressed in primary osteoblasts: *Htr1b*, *Htr2a*, and *Htr2b* (Supplementary Fig. S1D). HTR1B is the main serotonin receptor that controls osteoblast numbers (29). We thus analyzed the contribution of HTR1B to leukemia progression through the use of $Htr1b^{-/-}$ mice (30). WT $Htr1b^{+/+}$ mice injected with MLL/AF9 consistently developed leukemia and died within 14 to 19 days following transplantation (Fig. 1B), displaying splenomegaly (Fig. 1B), blast infiltration in BM, liver, and spleen (SP; Supplementary Fig. S1E), as well as peripheral blood neutrophilia, lymphocytopenia, and monocytosis (Supplementary Fig. S1F). In contrast, 100% of $Htr1b^{-/-}$ littermate mice examined ($n = 29$) remained leukemia-free for at least 90 days after transplantation, the entire time they were observed (Fig. 1B; Supplementary Fig. S1F). Upon harvest, all analyzed $Htr1b^{-/-}$ tissues were free of MLL/AF9 cells (Supplementary Fig. S1E).

In view of these observations, we asked at what stage during osteoblast differentiation is *Htr1b* expression necessary for leukemia progression. For this purpose, we inactivated *Htr1b* either in leptin receptor–expressing ($LepR^+$) mesenchymal stromal cells (MSC; ref. 31) or in osteoblasts. We found that ablating *Htr1b* expression in $LepR^+$ MSCs using the LepR-Cre line (32) did not hinder leukemia progression and lethality (Fig. 1C; Supplementary Fig. S1G). Next, we inactivated *Htr1b* in cells fully committed to the osteoblast fate using the collagen type I, alpha-1 (COL1A1)-Cre line (ref. 33; $Htr1b_{c\text{-}osb}^{-/-}$, Fig. 1D) or in differentiated osteoblasts using the osteocalcin (OCN)-Cre line (ref. 34; $Htr1b_{d\text{-}osb}^{-/-}$, Fig. 1E). In both scenarios, we observed a marked reduction in leukemia progression (Supplementary Fig. S1H and S1I) and either reduced mortality by 70% in $Htr1b_{c\text{-}osb}^{-/-}$ mice (Fig. 1D) or complete prevention of lethality in $Htr1b_{d\text{-}osb}^{-/-}$ mice (Fig. 1E) injected with MLL/AF9 cells, for the entire time that they were observed. In contrast, all WT control mice died within 14 to 17 days following MLL/AF9 transplantation. Recombination efficiency was twice as effective using OCN-Cre than COL1A-Cre (Supplementary Fig. S1J) at the $Htr1b^{fl/fl}$ locus, potentially explaining the difference in the level of protection against leukemia between the two conditional models. These data show that ablation of *Htr1b* in committed osteoblasts is sufficient to confer a close to complete protection against AML and to increase survival.

To determine whether *Htr1b* deletion in bone can limit AML progression after engraftment, we inducibly inactivated *Htr1b* following AML transplantation using the tetracycline-dependent *Tg(Sp7-tTA,tetO-EGFP/cre)1Amc/J* (Osx-Cre) line (35), which in adult mice deletes genes in cells at every stage of the osteoblast differentiation pathway. Delaying

Figure 1. Ablation of *Htr1b* in osteoblasts prevents AML progression. **A,** Survival curve of WT mice treated with vehicle ($n = 4$) or PTH ($n = 7$) and injected with MLL/AF9 AML cells. **B–E,** Survival curves of WT MLL/AF9-injected mice, their spleen weights, and representative epifluorescence images (radiance p/sec/cm^2/sr) of leukemia progression 14 days after MLL/AF9 injection in $Htr1b^{-/-}$ ($n = 29$) and $Htr1b^{+/+}$ littermates ($n = 13$; **B**); $Htr1b^{fl/fl}$; LepR-Cre: $Htr1b_{Lep\text{-}R}^{-/-}$ ($n = 8$) and $Htr1b_{Lep\text{-}R}^{+/+}$ littermates ($n = 6$; **C**); $Htr1b^{fl/fl}$; Col1a1-Cre: $Htr1b_{c\text{-}osb}^{-/-}$ ($n = 11$) and $Htr1b_{c\text{-}osb}^{+/+}$ littermates ($n = 12$; **B**)—the 4 $Htr1b_{c\text{-}osb}^{-/-}$ mice that developed leukemia are represented with red stars in the histogram of spleen weight and excluded from the statistical analysis; $Htr1b^{fl/fl}$; OCN-Cre: $Htr1b_{d\text{-}osb}^{-/-}$ ($n = 5$) and $Htr1b_{d\text{-}osb}^{+/+}$ littermates ($n = 10$; **E**). Orange arrow indicates the systematic genetic interrogation approach followed. **F,** Survival curve of $Htr1b^{fl/fl}$; Osx-Cre: $Htr1b_{Osx}^{-/-}$ (DOX removed 24 hours after MLL/AF9 injection; $n = 9$) and $Htr1b_{Osx}^{+/+}$ (kept on DOX, $n = 6$). **G,** Leukemia burden quantification (total flux, photons/sec) at day 12 after MLL/AF9 injection, $Htr1b_{Osx}^{+/+}$ (DOX, $n = 6$), $Htr1b_{Osx}^{-/-}$ (no DOX, $n = 9$). **H,** Survival curve of WT mice injected with MLL/AF9 cells and treated with either vehicle ($n = 10$) or the HTR1B antagonist SB224289 (SB9; $n = 10$). All survival curves shown are Kaplan–Meier curves with the *P* value of log-rank (Mantel–Cox) test between the indicated groups. All data are represented as mean ± SEM; statistical analysis done with an unpaired *t* test. *, $P \le 0.05$; **, $P \le 0.01$; ****, $P \le 0.0001$. See also Supplementary Fig. S1. DOX, doxycycline.

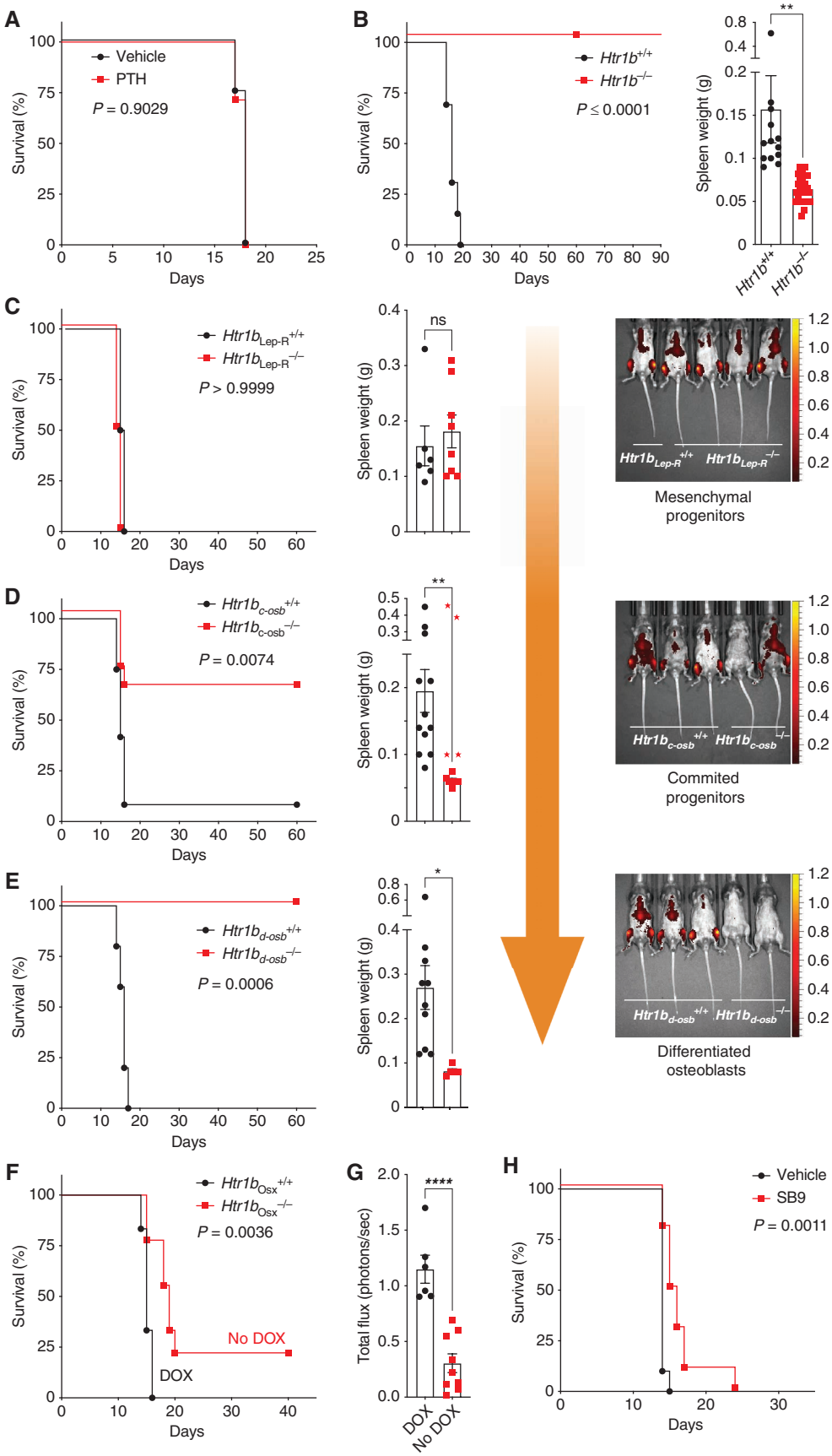

Osx-Cre expression until postnatally restricts deletion to committed osteoblasts (36, 37); therefore, *Htr1b*$^{fl/fl}$; *Osx-Cre* mice were born, weaned, and kept on doxycycline-containing diet to suppress transgene activation. Doxycycline removal after MLL/AF9 injection in *Htr1b*$^{fl/fl}$; *Osx-Cre* mice increased survival (Fig. 1F) and decreased leukemia burden (Fig. 1G; Supplementary Fig. S1K). Moreover, two mice showed complete protection against leukemia and survived the entire period of observation (Fig. 1F). Detailed analysis of their leukemia burden showed increasing signal up to day 12 after transplantation followed by a steady decrease to basal levels, which signifies complete clearance from AML (Supplementary Fig. S1SL). These results suggest that activation of pathways channeled through HTR1B in osteoblasts by AML cells is a prerequisite to allow leukemia growth in the BM. Moreover, inhibition of HTR1B signaling in osteoblasts after AML engraftment can limit—and in some cases clear—the disease, improving leukemia burden and survival.

The inhibition of AML progression following *Htr1b* inactivation in osteoblasts was surprising in view of the limited protection against AML induced by pharmacologic inhibition of serotonin synthesis previously observed (19). In that work, 30% reduction in serum 5-HT levels delayed AML progression and prolonged survival, but did not rescue the leukemic mice. To address if the partial rescue observed was due to the limited decrease in serum 5-HT levels, we examined whether the selective HTR1B receptor antagonist SB224289 (SB9; ref. 38) could confer a protective effect of a magnitude similar to that observed upon inactivation of *Htr1b* in osteoblasts. However, as seen following pharmacologic inhibition of 5-HT synthesis (19), SB9 only partially protected MLL/AF9–injected mice (Fig. 1H). Although SB9-treated mice injected with MLL/AF9 showed a significant increase in survival as compared with vehicle-treated ones (Fig. 1H), they eventually developed leukemia and died. Importantly, the administered SB9 dose was effective in abolishing 5-HT binding to HTR1B (Supplementary Fig. S1M). SB9 successfully inhibited 5-HT signaling because expression of Cyclins D1, D2, and E1 (suppressed upon 5-HT signaling through HTR1B in bone; ref. 29) was upregulated in the bone of SB9-treated mice (Supplementary Fig. S1N). As a control, expression of *Col1a1*, an osteoblast-specific gene, was not affected by SB9 treatment (Supplementary Fig. S1N). Therefore, SB9 treatment efficiently antagonized 5-HT signaling. The partial rescue from AML progression by either inhibition of 5-HT synthesis (19) or signaling (SB9), as compared with the close to complete protection seen after genetic *Htr1b* ablation, suggested that the main proleukemic effect of HTR1B may be mediated through a ligand different from serotonin.

AML Cells Preferentially Convert Trp into Kyn

To examine in a disease-relevant approach whether AML cells engage HTR1B in osteoblasts through a ligand different from serotonin, we leveraged an *in vitro* system using primary human osteoblasts from healthy individuals cocultured with a human AML cell line (OCI-AML3). To assess the contribution of secreted soluble factors that may act as HTR1B putative ligands, untargeted metabolomic profiling was performed on supernatants from either cell type alone or in coculture, using a panel of 466 metabolites (Supplementary Fig. S2A and S2B). We focused on those with coefficient of variation (CV) below 30% and integrated the data to identify metabolites showing a stronger combination of fold change and statistical significance. Our strategy was to first identify metabolites highly secreted by AML cells and not by osteoblasts (Fig. 2A), and then to select those displaying significant changes in their levels following coculture (Fig. 2B). This two-step analysis pinpointed one metabolite: Kyn. Not only were the levels of Kyn increased by 20-fold in supernatants from AML cells as compared with osteoblasts (see arrow in Fig. 2A) but, at the same time, it was the metabolite whose secretion by AML cells was most decreased after coculture with osteoblasts (see arrow in Fig. 2B). Kyn, like serotonin, is a major Trp catabolite. Although the ubiquitous indoleamine 2,3-dioxygenases (IDO1/IDO2) or the hepatic tryptophan 2,3-dioxygenase (TDO) enzymes catalyze conversion of Trp into Kyn, tryptophan hydroxylase-1 (TPH1) catalyzes the production of duodenal serotonin also from Trp (Fig. 2C). Trp levels were similar among all the supernatants analyzed (Fig. 2D). Interestingly, 5-HT levels were below the limits of detection, and the levels of the 5-HT metabolite 5-hydroxytryptophan (5-HTP) were not altered in coculture supernatants (Fig. 2D). These observations were further validated by liquid chromatography–mass spectrometry (LC/MS) targeted assays (Supplementary Fig. S2C).

A stringent analysis focusing on the metabolites with CV < 15% revealed that, similar to Kyn, pyridoxal-5′-phosphate (PLP; the active form of vitamin B_6) was increased 29-fold in supernatants from AML cells as compared with osteoblasts (Fig. 2E, gray histogram), and after Kyn it was the second most highly decreased metabolite upon coculture of AML with osteoblasts (Fig. 2E, blue histogram; Supplementary

Figure 2. Kynurenine (Kyn) is an oncometabolite increased in the BM niche of patients with MDS and AML that binds to HTR1B. **A** and **B,** Volcano plots for metabolites with CV <30% comparing OCI-AML3 cells untreated (AML) and human osteoblasts (hOsb; **A**) or AML cells untreated versus cocultures (24 hours). In **B**, arrows point to Kyn. **C,** Tryptophan (Trp) catabolism scheme. **D,** Relative abundance of Trp and its catabolic metabolites: Kyn, serotonin (5-HT), and 5-hydroxytryptophan (5-HTP) in the indicated supernatants at 24 hours ($n = 6$); two-way ANOVA. **E,** Heat map of the first 30 metabolites with CV <15% and histograms of fold induction (FI) of AML versus hOsb (gray) or AML versus coculture (blue). **F,** Violin plots of Kyn/Trp ratio levels in serum circulating levels of control-injected ($n = 19$) versus MLL/AF9-injected ($n = 28$) mice; unpaired *t* test. **G,** Violin plots of Kyn/Trp ratio levels in BM plasma from healthy donors ($n = 27$), MDS ($n = 30$), and AML ($n = 24$) patients; one-way ANOVA. **H,** Kyn/Trp levels in paired BM plasma samples at MDS stage and its corresponding transformed AML stage ($n = 6$); paired *t* test. **I,** RNA-sequencing analysis of BM-MNCs from patients with MDS ($n = 30$) and AML ($n = 30$) patients (TPM) for *TPH1* and *IDO1*; two-way ANOVA. **J,** *IDO1/TPH1* mRNA ratio in BM-MNCs from healthy donors ($n = 32$), patients with MDS ($n = 10$), and patients with AML ($n = 20$); one-way ANOVA. **K,** Concentration dependence of the Kyn-mediated competition of [^{3}H]-5-HT (25 nmol/L, 41.3Ci/mmol) binding by HEK293T membranes overexpressing the mouse ($n = 4$ experiments) or the human receptor ($n = 2$ experiments), yielding an IC_{50} of 54.1 μmol/L and 24.4 μmol/L, respectively (see Table 1 for details). **L,** $G_{i/o}$-mediated cAMP inhibition assays ($n = 14$). **M,** Binding of [^{3}H]-5-HT (25 nmol/L, 41.3 Ci/mmol) or [^{3}H]-Kyn (50 μmol/L, 0.125 Ci/mmol) was measured with *Htr1b*-overexpressing HEK293T membranes in the presence of increasing concentrations of SB9 ($n = 4$). Nonlinear regression fitting was used to fit the isotherms, and the best-fit values and statistics of the fit are shown in Table 1. All data are expressed as mean ± SEM. *, $P \le 0.05$; **, $P \le 0.01$; ***, $P \le 0.001$; ****, $P \le 0.0001$. See also Supplementary Fig. S2 and Table 1.

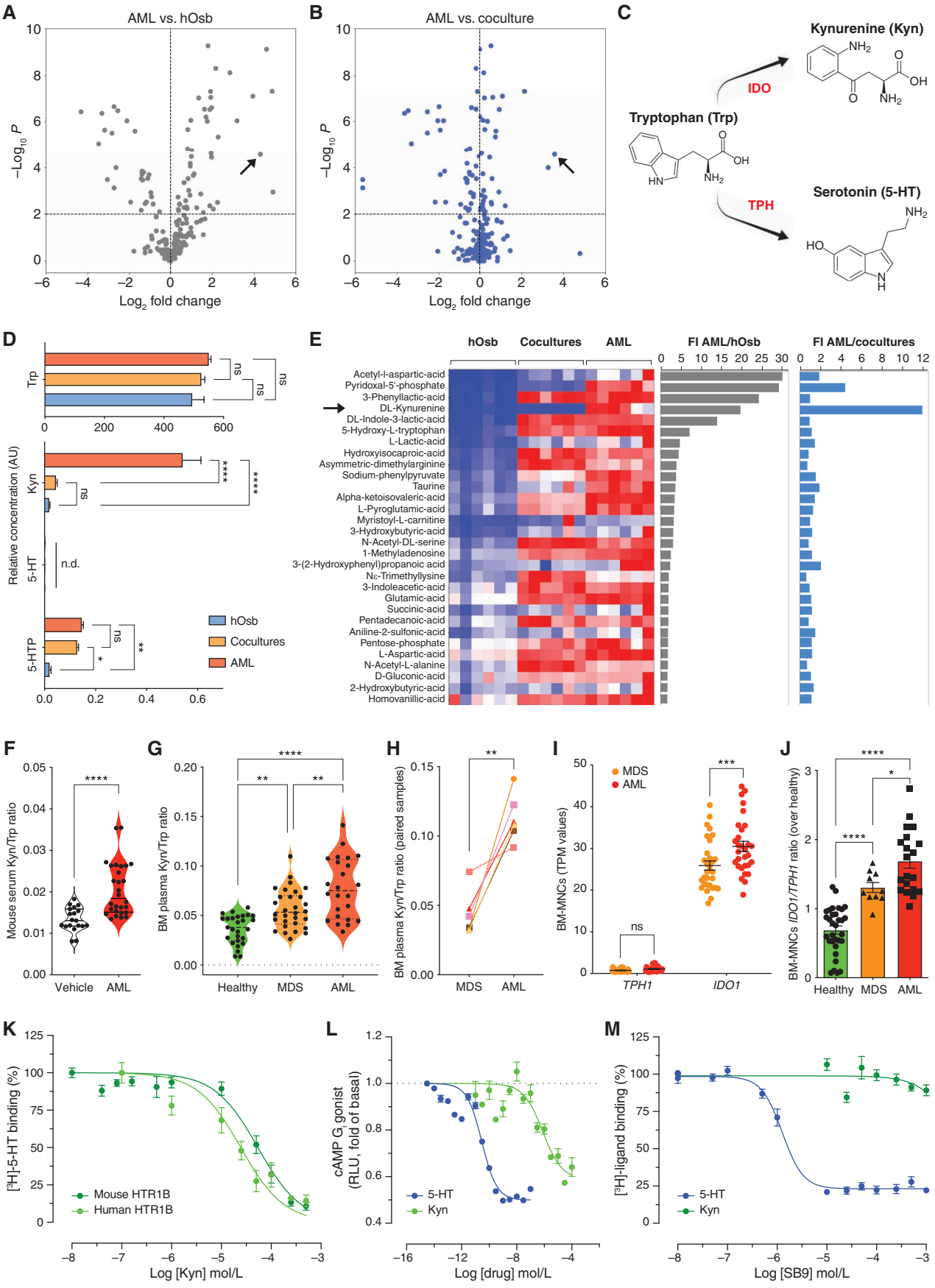

Table 1. Competition binding and functional radioligand assays

Figure	HTR1B species	Radiolabeled compound	Competing compound	IC_{50} (μmol/L)	Log IC_{50} (mol/L) Value	SEM
2K	Mouse	[^{3}H]-5-HT	Kyn	54.091	–4.267	0.052
	Human			24.444	–4.612	0.071
2M	Mouse	[^{3}H]-5-HT	SB224289	1.2703	–5.896	0.049
		[^{3}H]-5-Kyn		7,720.9	–2.112	0.961
S2J	Mouse	[^{3}H]-5-HT	5-HT	0.0811	–7.091	0.005
	Human			0.0597	–7.224	0.076
				K_i (μmol/L)	Log K_i (mol/L)	
S2K	Human	[^{3}H]-GR125743	Kyn	17.306	–4.762	0.051
			5-HT	0.0156	–7.808	0.021
			Ergotamine	0.0006	–9.246	0.020
				EC_{50} (nmol/L)	Log EC_{50} (mol/L)	
2L	Human	cAMP G_i agonist	5-HT	0.0298	–10.526	0.038
			Kyn	771.68	–6.113	0.206

NOTE: Related to Fig. 2 and Supplementary Fig. S2. The values shown are the mean ± SEM.

Abbreviations: IC_{50}, Half-maximal inhibitory concentration; K_i, inhibitory constant; EC_{50}, half-maximal effective concentration.

Fig. S2D and S2E). PLP is a necessary cofactor for more than 160 enzymes (reviewed in ref. 39), including several in the Kyn pathway, suggesting that its downregulation may be another means of Kyn depletion in the presence of osteoblasts. Remarkably, blockade of the vitamin B_6 metabolic pathway in AML cells exhibits antileukemic activity (40), supporting the idea that depletion of Kyn synthesis in AML cells is an important mechanism to hinder AML progression. However, whether the antileukemogenic activity of PLP also involves depletion of Kyn levels would need to be further explored.

High Kyn Levels Are a Hallmark of MDS and AML

To determine the *in vivo* significance of Kyn in AML, we measured circulating Kyn and Trp levels in leukemic mice and confirmed that the Kyn-to-Trp ratio (an indicator of IDO1 activity) was elevated in the peripheral blood serum of mice injected with MLL/AF9 cells as compared with control, vehicle-injected mice (Fig. 2F; Supplementary Fig. S2F). To assess if our findings *in vitro* and in murine models were recapitulated in human leukemia, specifically within the BM niche compartment, we examined whether induction of Kyn secretion is a broad feature of AML or the patients with preleukemic MDS (Supplementary Table S1). We found that the Kyn/Trp ratio within the BM plasma of patients with MDS and patients with AML was significantly higher than in age-matched healthy controls (Fig. 2G; Supplementary Fig. S2G and S2H). Moreover, we compared Kyn/Trp ratio levels within the BM plasma of paired MDS and progressed-to-AML patient samples: In the six paired samples analyzed, Kyn/Trp ratio levels were increased in the BM plasma at the AML stage as compared with their MDS-stage sample (Fig. 2H), suggesting that increased Kyn production correlates with disease progression.

RNA-sequencing (RNA-seq) analysis of BM mononuclear cells (BM-MNC) from patients with MDS and patients with AML showed that whereas *TPH1* expression is very low [0.74 ± 0.06 in MDS and 1.09 ± 0.11 in AML, transcripts per million (TPM)], expression of *IDO1* is much higher (25.89 ± 1.12 MDS and 30.48 ± 1.22 AML; Fig. 2I; Supplementary Table S1). Quantitative PCR analysis of BM-MNCs of additional independent cohorts of healthy subjects, patients with MDS, and patients with AML identified a similar progressive increase in the *IDO1/TPH1* ratio from healthy controls as compared with patients. Moreover, this increase was similarly observed along progression of disease severity from MDS to AML (Fig. 2J).

Collectively, these results identify Kyn as an oncometabolite, demonstrating preferential catabolism of Trp toward the Kyn pathway in cells of patients with MDS and patients with AML, as well as increased levels of the metabolite in their BM plasma. A progressive increase in Kyn production appears to occur as the disease pathogenesis proceeds from MDS to AML.

Kyn Binds to and Regulates HTR1B Signaling

The increased and preferential production of Kyn over 5-HT by leukemic cells, together with the partial protective effect caused by the HTR1B antagonist SB9, prompted us to examine whether Kyn could be a previously unappreciated ligand of HTR1B. To address whether Kyn is a serotonin receptor ligand, we performed competition binding and functional assays on HEK293T cells overexpressing mouse or human HTR1B (Supplementary Fig. S2I). Kyn was able to compete the binding of 25 nmol/L [^{3}H]-5-HT to mouse (IC_{50} of ~54 μmol/L) and human (IC_{50} of ~24 μmol/L) HTR1B (Fig. 2K; Table 1) in membranes of HEK293T cells overexpressing the murine or human receptor, respectively; as a control, 5-HT showed similar competitive binding activity for both receptors (Supplementary Fig. S2J; Table 1). Similarly, Kyn competed the binding of the potent serotonin receptor antagonist [^{3}H]-GR125743 to HTR1B with a K_i of ~17 μmol/L (Supplementary Fig. S2K; Table 1) in membranes isolated from HEK293T cells stably overexpressing

the human *HTR1B*. Moreover, and in agreement with its binding properties, Kyn acts as a partial agonist of $G_{i/o}$-mediated cAMP production through HTR1B with an EC_{50} of ~772 nmol/L (Fig. 2L; Table 1).

As SB9 used to displace 5-HT binding to HTR1B was not able to effectively hinder AML *in vivo* (Fig. 1H), we examined whether it could displace Kyn binding to HTR1B. However, at a concentration equal to the one administered *in vivo* (~90 μmol/L; Fig. 1H), SB9 had no effect on Kyn binding to the murine HTR1B receptor (Fig. 2M). Altogether, these experiments demonstrate that Kyn is a partial agonist of HTR1B in both mouse and human, able to regulate its signaling.

Genetic Inhibition of Kyn Production Hinders AML Progression

To explore *in vivo* the significance of Kyn for leukemia progression, we inhibited its synthesis by suppressing IDO1 activity in mouse and human AML cells. We used a CRISPR/Cas9 editing strategy designing a series of different single-guide RNAs (sgRNA) targeting *Ido1* exons 3 and 4, which encode critical portions of the enzyme catalytic site and are common to all IDO isoforms (Supplementary Fig. S3A).

First, *Ido1* was genetically ablated in the myelomonocytic leukemia cell line WEHI-3B. High deletion efficiencies were achieved on WEHI-3B cells, especially when combining two sgRNAs targeting exon 3 (Supplementary Fig. S3B; Supplementary Data S1A). Mice receiving the Cas9-only WEHI-3B control cells died within 2.5 weeks after injection, whereas the ones injected with sgRNA#146 alone or in combination with sgRNA#196 showed significant increased survivals (Supplementary Fig. S3C). Importantly, the decrease in Kyn levels (Supplementary Fig. S3D) as well as the protective effect of *Ido1* deletion was proportional to the efficiency of *Ido1* deletion.

Next, we used sgRNAs targeting *Ido1* exons 3 and 4 to modify primary murine leukemia cells. *Ido1* exon 3–edited MLL/AF9 cells (Supplementary Data S1B) were transplanted into WT nonirradiated recipients, and leukemia progression was monitored (Fig. 3A; Supplementary Fig. S3E). Although all mice receiving the Cas9-only MLL/AF9 control cells died within three weeks after injection (Fig. 3B), *Ido1* deletion significantly attenuated (sgRNA#203 and sgRNA#196, ~40% deletion efficiency) or even abrogated (sgRNA#146, ~56% deletion efficiency) disease progression (Supplementary Fig. S3E) and decreased serum Kyn levels (Supplementary Fig. S3F), extending overall survival (Fig. 3B).

CRISPR/Cas9-mediated *Ido1* targeting of exon 4 (Supplementary Data S1C) achieved a 70% loss of expression of *Ido1* at the mRNA level (Fig. 3C). Injection of *Ido1*-sgRNA#610–edited MLL/AF9 cells into WT nonirradiated recipients led to a significant increase in survival (Fig. 3D). Thirty-six percent of the mice receiving the MLL/AF9-edited cells showed complete protection against leukemia progression and survived (Fig. 3D; Supplementary Fig. S3G). Notably, spleen weight (Supplementary Fig. S3H) and serum Kyn levels (Supplementary Fig. S3I) were proportional to the decrease in *Ido1* levels as well as to the survival effects. Because the majority of MLL/AF9 cells (~70%) were efficiently targeted by sgRNA#610, we reasoned that the small residual fraction of unedited AML cells would outcompete edited cells over time. Indeed, sequencing analysis of BM cells from moribund mice showed that IDO1 activity was not compromised in 45% of the mice, which exhibited a percentage of unedited (WT) sequence between 60% and 100% (Supplementary Fig. S3J). These results suggested that the few unedited cells present in the initially injected population had a clonal advantage over the *Ido1*-edited ones and were responsible for disease progression. Only two of the nonrescued mice showed <10% unedited cells; however, in one of them (BM#19) an in-frame deletion may have preserved IDO1 functionality, allowing AML to progress, whereas in the other one (BM#12) a disrupted IDO1 frameshift might explain its prolonged survival (Supplementary Fig. S3J).

The relevance of IDO1 in the progression of human leukemia was tested using the OCI-AML3 AML cell line. OCI-AML3 cells nucleofected with Cas9 and the combination of sgRNA#126 and sgRNA#170 (targeting exon 3 of *IDO1*) showed high deletion efficiency (~85%; Fig. 3E; Supplementary Data S1D) and when exposed to IFNγ—a strong inducer of *IDO1*—CRISPR/Cas9-targeted OCI-AML3 cells failed to upregulate its expression (Fig. 3F). Transplantation of OCI-AML3 *IDO1*-targeted cells into sublethally irradiated NOD.Cg-*Prkdc*^{scid} *Il2rg*^{tm1Wjl}/SzJ (NSG) mice (Fig. 3G) resulted in delayed disease progression as seen by a ~60% decrease in BM AML burden, ~20% decrease in SP AML burden, and significantly reduced spleen weights (Fig. 3H). Consistent with the decreased AML burden, the level of *IDO1* expression in BM of NSG mice at harvest showed a 73% decrease compared with control (Cas9-only) injected mice (Supplementary Fig. S3K), confirming that a possible outgrowth of a reversion mutant was residual. Additionally, serum Kyn levels were reduced by ~30% (Supplementary Fig. S3L). Of note, although OCI-AML3 *IDO1*-targeted cells did not show any intrinsic proliferative defect as compared with the control (Cas9 only) ones (Supplementary Fig. S3M), their proliferation was decreased when placed in cocultures with primary human osteoblasts (Fig. 3I). In contrast, simulating the *IDO1* upregulation triggered by osteoblasts, overexpression of *IDO1* in OCI-AML3 cells (Supplementary Fig. S3N) promoted their proliferation in a dose-dependent manner (Supplementary Fig. S3O). These results suggest that the *in vivo* AML growth disadvantage when *IDO1* is depleted is osteoblast-related.

Taken together, these results demonstrate that IDO1 is required to sustain AML cell proliferation in an osteoblast-dependent manner, and that genetic ablation of *IDO1* suppresses AML growth in a dose-dependent manner, suggesting that disease severity is inversely correlated to the expression of *Ido1*.

AML Cells Induce a Self-Reinforcing Osteoblastic Niche through SAA1-Mediated *IDO1* Upregulation in an HTR1B-Dependent Manner

Next, we sought to identify the downstream molecular targets of Kyn in human osteoblasts that render the BM niche permissive to AML engraftment and support proliferation of leukemia cells. For this purpose, and to closely compare our studies in mice and humans, we used the human THP-1 AML cell line, which carries the MLL/AF9 fusion oncogene, the most commonly involved in MLL translocations and a powerful driver of tumor progression. We characterized the transcriptional profile of cocultures of THP-1 cells with

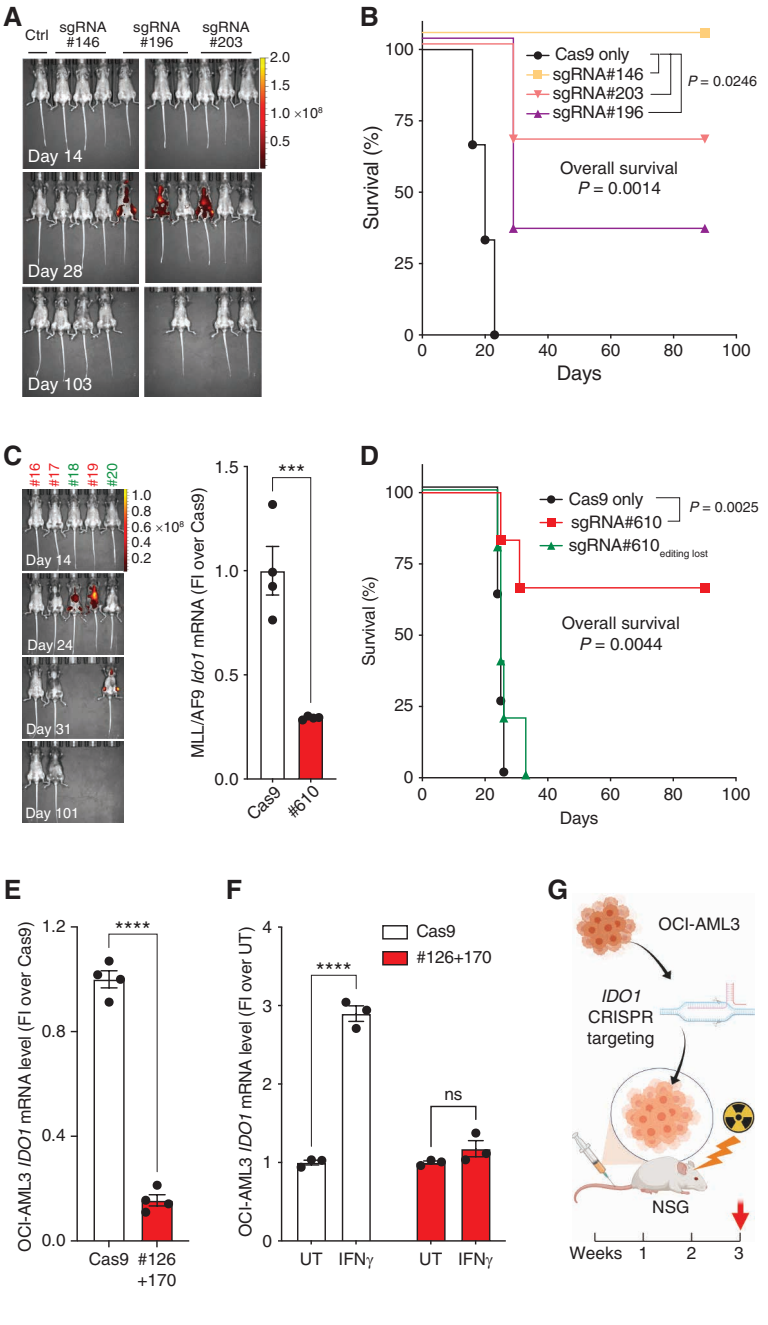

Figure 3. Genetic inhibition of kynurenine (Kyn) production hinders AML progression. **A,** Representative epifluorescence images of leukemia progression in WT mice injected with MLL/AF9-CRISPR/Cas9-edited cells (sgRNAs: #146, #196 and #203; Ctrl: no leukemia). **B,** Survival curve of mice injected with the indicated sgRNAs MLL/AF9-edited or Cas9-only-MLL/AF9 control cells ($n = 3$ all groups). **C,** Representative epifluorescence images of leukemia progression in WT mice injected with MLL/AF9-CRISPR/Cas9-edited cells (sgRNAs: #610) and *Ido1* mRNA levels of MLL/AF9-sgRNA#610-edited cells before injection ($n = 4$); unpaired *t* test. **D,** Survival curve of WT mice injected with MLL/AF9-sgRNA#610-edited cells ($n = 11$) or Cas9 only control ($n = 9$). Mice showing > 60% of unedited (WT) sequence in their BM after harvesting are depicted as sgRNA#610$_{\text{editing lost}}$ (green; $n = 5$). **E,** *IDO1* mRNA levels in OCI-AML3 cells nucleofected with Cas9 and sgRN#610 used in transplant experiment. **F,** *IDO1* mRNA levels in OCI-AML3 cells exposed to IFNγ (overnight, 50 ng/mL, $n = 3$); two-way ANOVA. **G,** Outline of transplantation assay with OCI-AML3 CRISPR/Cas9-*IDO1*–targeted cells in NSG mice. **H,** AML burden in BM, SP, and spleen weight (mg)—referred to as total body weight (g)—of NSG mice 3 weeks after injection of OCI-AML3 cells ($n = 8$, Cas9; $n = 10$, #126+170). **I,** Proliferation of OCI-AML3 cells upon 72 hours of coculture with primary human osteoblasts ($n = 7$). Survival curves are Kaplan–Meier with *P* value of log-rank (Mantel–Cox) test between the indicated groups. All data are expressed as mean ± SEM. Statistical analysis done with unpaired *t* test unless otherwise stated. **, $P \leq 0.01$; ***, $P \leq 0.001$; ****, $P \leq 0.0001$. See also Supplementary Fig. S3 and Supplementary Data S1.

primary human osteoblasts and integrated the data to identify cross-talk signals. RNA-seq analysis showed that 137 genes were significantly differentially expressed in osteoblasts exposed to AML cells as compared with osteoblasts cultured alone. Among those, pathway enrichment analysis identified several inflammatory pathways regulating multiple aspects of innate and adaptive immune functions (NFκB, TNF, and IL17 signaling pathways) that were significantly increased in osteoblasts exposed to AML cells (Supplementary Fig. S4A). In agreement with these observations, leukemic cells increased *NFκB1A* expression (Supplementary Fig. S4B) and induced p65 translocation to the nucleus (Supplementary Fig. S4C) in primary osteoblasts isolated from healthy subjects, indicating that AML cells activate canonical NFκB signaling in osteoblasts. Indeed, gene set enrichment analysis (GSEA) focused on genes encoding secreted molecules demonstrated that expression of several proinflammatory cytokine and chemokine genes in the NFκB pathway was highly upregulated in primary human osteoblasts exposed to AML cells (Fig. 4A; Supplementary Fig. S4D). This proinflammatory signature elicited in osteoblasts by AML cells was confirmed by qRT-PCR in primary osteoblasts from healthy human subjects cocultured with the THP-1 or OCI-AML3 AML cell lines (Supplementary Fig. S4E and S4F). Selected targets were additionally validated through multiplex assessment of protein levels in the corresponding supernatants (Supplementary Fig. S4G). Of note, an apoptosis pathway signature was upregulated in osteoblasts exposed to AML cells (Supplementary Fig. S4H), and this upregulation correlated with an inflammatory signature in leukemic cells exposed to osteoblasts (Supplementary Fig. S4I), suggesting that an inflammation-induced apoptosis pathway may be the mechanism responsible for bone loss in AML.

More specifically, a parallel RNA-seq analysis of the THP-1 AML cells exposed to human primary osteoblasts showed increased expression of *IDO1* (log fold change 4.6), but no change in *TPH1* expression (Fig. 4B). Interestingly, following the initial differential expression analysis, a pathway enrichment analysis highlighted several IDO1-activating pathways (Supplementary Fig. S4J). GSEA showed that Trp catabolism as well as the Kyn pathway itself were upregulated in THP-1 cells exposed to osteoblasts (Supplementary Fig. S4K), and qRT-PCR analysis confirmed *IDO1* upregulation (Supplementary Fig. S4L). Notably, genetic ablation of *IDO1* by CRISPR/Cas9 editing in OCI-AML3 cells abrogated the osteoblast-induced upregulation of *IDO1* expression observed in the AML cells upon coculture with primary human osteoblasts (Supplementary Fig. S4M). Taken together, these results suggest that AML cells "prime" osteoblasts to secrete factors that stimulate *IDO1* expression.

In order to pinpoint these factors, we directly examined whether any of the proinflammatory candidate molecules identified to be elicited in primary human osteoblasts by AML cells (Fig. 4A; Supplementary Fig. S4E–S4G) affected *IDO1* expression in the latter. Among them, the rapidly induced (Supplementary Fig. S4N) acute-phase protein serum amyloid A1 (SAA1) was the only osteoblast-secreted molecule able to upregulate *IDO1* expression in OCI-AML3 leukemic cells (Fig. 4C). Most importantly, the ability of SAA1 to upregulate *IDO1* expression was observed across several human AML cell lines as well as the MDS-L cell line (Supplementary Fig. S4O).

SAA1 is the functional human ortholog of murine *Saa3* (41). Similar to SAA1, SAA3 is an acute-phase response protein highly induced during inflammation by IL1β, TNFα, and IL6 through NFκB signaling (42). Of interest, these cytokines as well as the NFκB pathway itself were found to be significantly upregulated in the RNA-seq data set of human osteoblasts exposed to AML cells (Fig. 4A; Supplementary Fig. S4D–S4G). To assess if our findings in human cells were recapitulated in the mouse model, we examined whether *Ido1* upregulation was a general consequence of SAA exposure. We found that, as it is the case in human AML cells exposed to SAA1 (Fig. 4C; Supplementary Fig. S4O), recombinant mouse SAA3 upregulated *Ido1* expression in murine WEHI-3B AML cells (Fig. 4D). Moreover, recombinant human SAA1 was also able to upregulate *Ido1* expression in WEHI-3B cells with a magnitude similar to SAA3 (Fig. 4D), underscoring the notion that this mode of regulation is conserved in mice and humans.

To test whether the AML-elicited SAA response observed in osteoblasts was dependent on Kyn engagement of HTR1B, we used mouse primary osteoblasts isolated from *Htr1b*$^{-/-}$ or *Htr1b*$^{+/+}$ littermate mice. Notably, whereas both Kyn and WEHI-3B AML cells potently upregulated *Saa3* expression in mouse osteoblasts, 5-HT had no effect (Fig. 4E). More importantly, both Kyn and WEHI-3B cells failed to upregulate *Saa3* expression in *Htr1b*$^{-/-}$ primary osteoblasts (Fig. 4E). These results demonstrate that Kyn secreted by AML cells upregulates *Saa3* expression in osteoblasts in an HTR1B-dependent manner. This upregulation serves as a positive feedback mechanism to amplify *Ido1* expression in AML cells.

SAA1 Levels Are Elevated in Patients with MDS and Patients with AML and Correlate with Disease Progression and Kyn Levels

To determine the *in vivo* significance of *Saa3* in AML, we measured circulating SAA3 levels in leukemic mice and confirmed that they were elevated in the peripheral blood serum of mice injected with MLL/AF9 cells as compared with control, vehicle-injected mice (Fig. 4F). The relevance of these findings to the human disease was assessed by measuring SAA1 levels in the BM plasma of patients with MDS and patients with AML. In agreement with the increased mRNA expression of *SAA1* observed in osteoblasts upon exposure to AML cells (Fig. 4A; Supplementary Fig. S4E, S4F, and S4N), BM plasma levels of SAA1 were 6.4- and 10.6-fold times higher in patients with MDS and patients with AML, respectively, as compared with age-matched healthy subjects (Fig. 4G; Supplementary Fig. S4P). More importantly, SAA1 concentration in all the paired human samples analyzed was higher in the BM plasma of patients with transformed AML versus their paired previous MDS-stage samples (Fig. 4H), suggesting a role of SAA1 in AML pathogenesis. Interestingly, a correlation between Kyn/Trp ratio and SAA1 levels in BM plasma was observed along progression from MDS to AML (Fig. 4I), underscoring a potential prognostic value of the two biomarkers in MDS to AML progression.

SAA Selectively Promotes Proliferation of AML Cells

To this point, a compilation of data obtained from murine and human samples and models of AML or MDS demonstrates that leukemic cells stimulate a proinflammatory

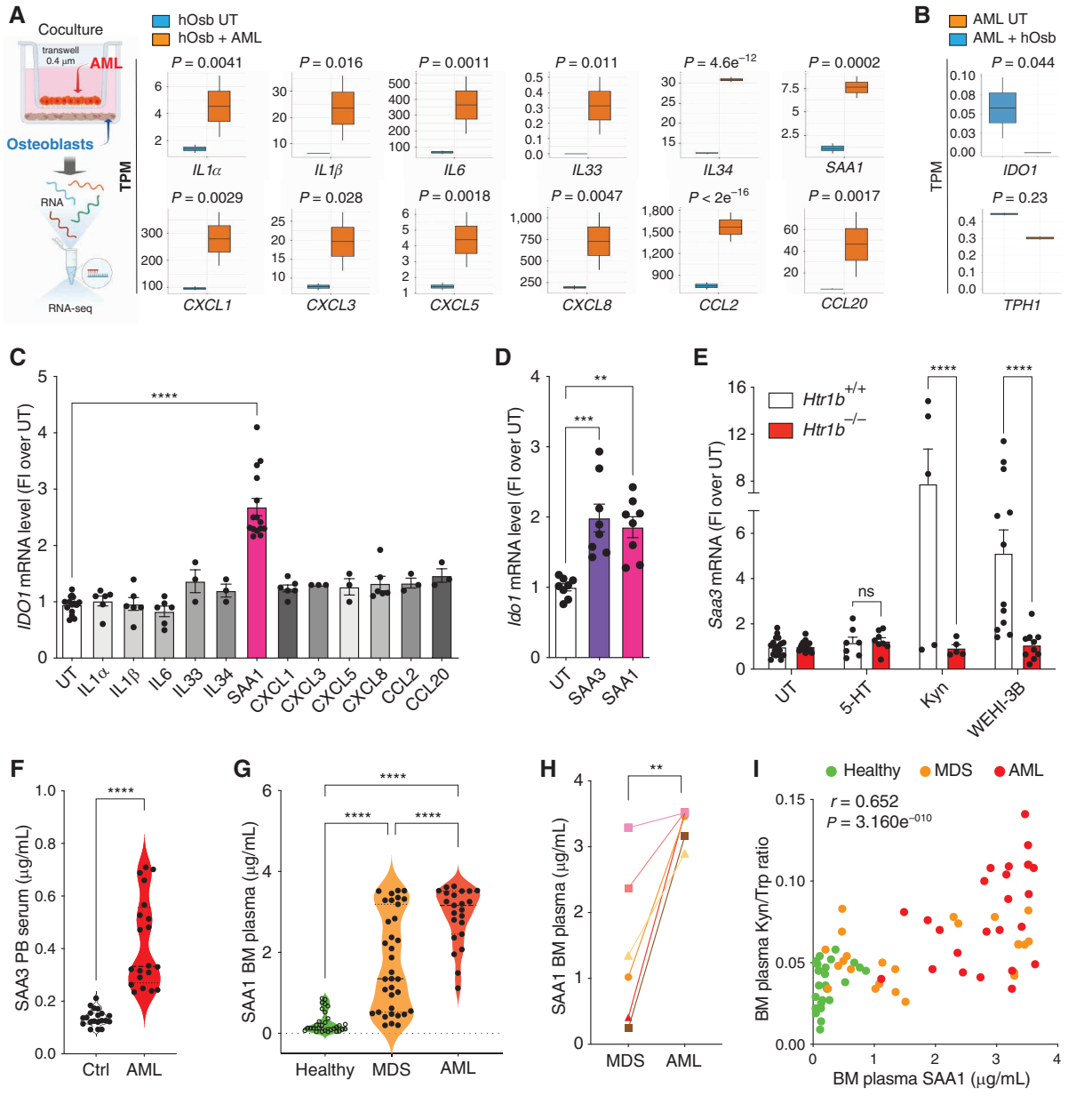

Figure 4. AML cells self-amplify Kyn production through HTR1B–SAA signaling in osteoblasts. **A,** Schematic of RNA-seq analysis strategy (left) and box plots (right) of the main secreted molecules significantly upregulated in primary human osteoblasts untreated (UT) or cocultured 24 hours with the THP-1 AML cell line ($n = 2$); Wald test, two-sided. **B,** Box plots for *IDO1* and *TPH1* from RNA-seq analysis of THP-1 cells exposed 24 hours to primary human osteoblasts ($n = 2$); Wald test, two-sided. **C,** *IDO1* mRNA levels in OCI-AML3 cells exposed overnight to the indicated molecules (UT and SAA1, $n = 15$; IL1α, IL1β, IL6, CXCL1, and CXCL8, $n = 6$; IL33, IL34, CXCL3, CXCL5, CCL2, and CCL20, $n = 3$). **D,** *Ido1* mRNA levels in WEHI-3B cells exposed overnight to recombinant mouse SAA3 or recombinant human SAA1 ($n = 8$). **E,** *Saa3* mRNA relative level in primary differentiated mouse calvaria from *Htr1b*$^{-/-}$ and *Htr1b*$^{+/+}$ littermates, exposed for 24 hours to 5-HT (25 nmol/L, $n = 7$–8), Kyn (25 nmol/L, $n = 5$), or the WEHI-3B cell line ($n = 10$–12); two-way ANOVA. **F,** Violin plots of SAA3 peripheral blood (PB) serum levels in control ($n = 20$) and MLL/AF9-injected mice ($n = 20$); unpaired *t* test. **G,** Violin plots of SAA1 BM plasma levels in healthy donors ($n = 30$), patients with MDS ($n = 35$), and patients with AML ($n = 23$). **H,** SAA1 BM plasma levels in paired samples from patients (MDS and corresponding AML-transformed stage; $n = 6$ paired samples); paired *t* test. **I,** Multiple variable data plot of BM plasma levels for SAA1 and Kyn/Trp ratio along healthy, MDS, or AML samples; Pearson correlation values are shown for Kyn/Trp ratio and SAA1 BM plasma levels. All data expressed as mean ± SEM. Statistical analysis was done with one-way ANOVA unless otherwise stated. **, $P \leq 0.01$; ***, $P \leq 0.001$; ****, $P \leq 0.0001$. See also Supplementary Fig. S4.

remodeling of the osteoblastic niche. This mechanism may be a means for leukemia to operate a positive feedback loop that self-reinforces its progression, specifically through SAA1-mediated, HTR1B-dependent upregulation of *IDO1*. To examine this hypothesis, we first tested the effect of SAA in leukemia cell proliferation. AML cell lines exposed to SAA1 (human) or SAA3 (mouse) showed an increased proliferation as compared with vehicle-treated ones (Fig. 5A; Supplementary Fig. S5A). Similarly, SAA1 promoted proliferation of lineage-depleted AML and MDS BM-MNCs isolated from patient aspirates (Fig. 5B). In parallel, *IDO1* mRNA levels were increased in all the patient-derived BM-MNCs upon SAA1 exposure (Fig. 5C).

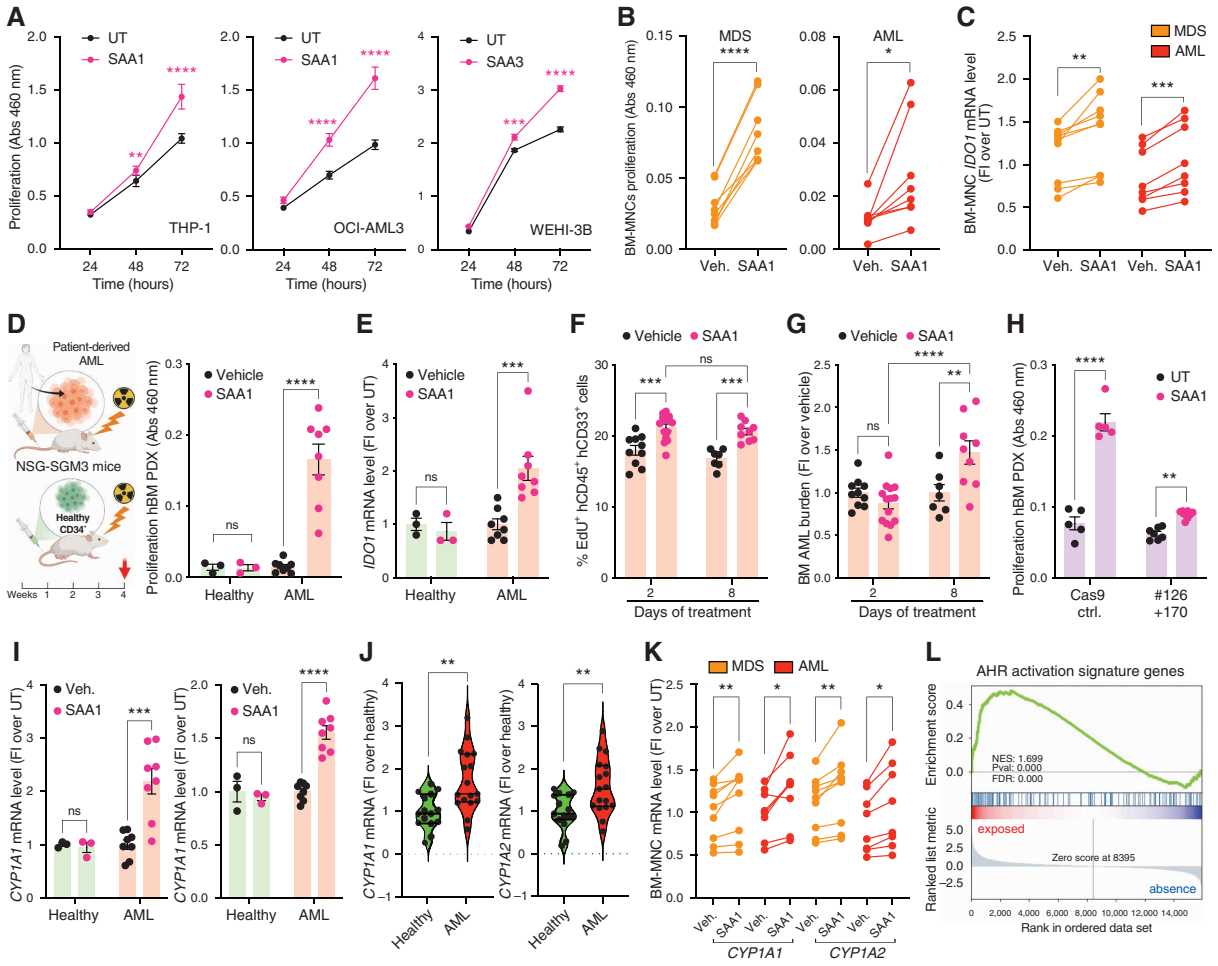

Figure 5. SAA1 selectively promotes leukemic cell proliferation by upregulating *IDO1* expression through activation of the aryl hydrocarbon receptor (AHR) pathway. **A,** Proliferation of human THP-1 and OCI-AML3 ($n = 22$) and mouse WEHI-3B ($n = 8$) AML cell lines exposed to SAA1 or SAA3, respectively (1 μg/mL, 24–72 hours). Proliferation (**B**) and *IDO1* mRNA levels (**C**) of human BM-MNCs isolated from MDS or AML (lineage-depleted) BM aspirates ($n = 8$) and exposed to SAA1 (5 μg/mL, 24 hours), paired *t* test. **D,** Left, schematic of PDX model used. Right, proliferation of total human BM cells isolated from the PDX mice injected with either healthy CD34$^+$ ($n = 3$) or patient-derived AML cells ($n = 8$) exposed to vehicle (PBS) or SAA1 (1 μg/mL, 24 hours). **E,** *IDO1* mRNA level from cells in **D**; two-way ANOVA. *In vivo* proliferation of leukemic blasts (hCD45$^+$CD33$^+$; **F**) and BM AML burden (**G**) in mice treated for 2 or 8 days with either vehicle ($n = 10$ and $n = 7$, respectively) or SAA1 ($n = 14$ and $n = 9$, respectively); two-way ANOVA. **H,** Proliferation of total human AML BM cells isolated from PDX mice and nucleofected with Cas9 ($n = 5$) or Cas9 and the combination of sgRNA#126 and sgRNA#170 ($n = 8$) exposed to vehicle or SAA1 (1 μg/mL, 24 hours); two-way ANOVA. **I,** mRNA level of *CYP1A1* and *CYP1A2* from cells in **D**; two-way ANOVA. **J,** Violin plots for mRNA levels of *CYP1A1* and *CYP1A2* in BM-MNCs from healthy donors ($n = 15$) and patients with AML ($n = 17$). **K,** *CYP1A1* and *CYP1A2* mRNA levels from cells in **B**. **L,** GSEA of AHR activation signature genes in THP-1 cells cocultured with human osteoblasts for 24 hours. All data expressed as mean ± SEM. Statistical analysis was done with an unpaired *t* test unless otherwise stated. *, $P \le 0.05$; **, $P \le 0.01$; ***, $P \le 0.001$; ****, $P \le 0.0001$. See also Supplementary Fig. S5.

To better understand the SAA-induced AML proliferative activity *in vivo*, we took advantage of a PDX model. Sublethally irradiated NSG-SGM3 (NSGS) mice were injected with either healthy human CD34$^+$ cells (PDX healthy) or patient-derived AML cells (PDX AML), achieving a human engraftment range between 6% and 23% for the former and 43% to 65% for the latter, four weeks after injection (Supplementary Fig. S5B). Following BM isolation and CD45$^+$ mouse cell depletion, total BM human cells were cultured and exposed to SAA1 for 24 hours. Although human cells from CD34$^+$ healthy injected mice were unresponsive to SAA1, patient-derived cells from AML-injected mice displayed a high proliferative activity as compared with their vehicle-treated counterparts (Fig. 5D). Notably, *IDO1* expression was upregulated only in response to SAA1 in the PDX AML-isolated human cells (Fig. 5E), mimicking our observations with patient-derived *ex vivo* cultures (Fig. 5C) and indicating that SAA1 induces at the same time *IDO1* expression and proliferation of leukemia cells but not of healthy CD34$^+$ cells.

To determine whether the SAA proproliferative activity observed *in vitro* and *ex vivo* was also reproduced *in vivo*, we treated PDX mice with recombinant human SAA1. SAA1 was administered intravenously (i.v.) at an equimolar dose to the one used for the *in vitro* and *ex vivo* assays for 2 or 8 days (Supplementary Fig. S5C). Three hours before harvest, mice were injected with 5-ethynyl-2′-deoxyuridine (EdU) to analyze *in vivo* leukemic blast cell cycle. SAA1 treatment yielded a maintained and prominent increase in the proliferative rate of leukemic blasts (hCD45$^+$ CD33$^+$) after the 2- and 8-day treatments as shown by the increase in EdU$^+$ cells (S-phase;

Fig. 5F) and the decrease in the G_0–G_1 cells, whereas the G_2–M phase was unvarying (Supplementary Fig. S5D). In addition, 8-day treatment with SAA1 promoted survival of leukemic blasts (reduced the percentage of sub-G_1 apoptotic cells; Supplementary Fig. S5D). Cumulatively, the increased proliferating rate and the decrease in apoptosis of leukemic blasts led to a 1.5-fold increase in AML burden in the BM at the completion of the 8-day treatment period (Fig. 5G).

To unequivocally assess whether the proliferation increase observed upon SAA exposure was a direct consequence of the concomitant upregulation of *IDO1* expression, we performed CRISPR/Cas9 targeting of *IDO1* in primary human AML cells isolated from the PDX model, achieving ~70% deletion efficiency (Supplementary Fig. S5E; Supplementary Data S1E). Upon SAA1 exposure, *IDO1*-edited primary human AML cells failed to upregulate *IDO1* expression as compared with control (Cas9 only) cells (Supplementary Fig. S5F). More importantly, *IDO1*-targeted cells showed a 2-fold decrease in their proliferation rate in response to SAA1 as compared with control cells (Fig. 5H). Conversely, injection of Kyn in low AML burden PDX mice (to distinguish the stimulatory effect of exogenous Kyn from that of AML cells) increases serum SAA3 (Supplementary Fig. S5G) as well as the proliferative capacity of the leukemic blasts (Supplementary Fig. S5H). As a consequence, AML burden increased in BM and SP of the Kyn-treated group (Supplementary Fig. S5I).

These results suggest that SAA specifically promotes proliferation and cell-cycle progression of leukemia cells. Moreover, SAA-induced proliferation occurs through upregulation of *IDO1* expression.

SAA Engages the AHR Pathway to Increase *IDO1* Expression

Because upregulation of *IDO1* expression will trigger Kyn synthesis, we examined whether the Kyn-induced SAA1 secretion stimulates AML proliferation by activating Kyn signaling in AML cells. Kyn is an endogenous agonist of the aryl hydrocarbon receptor (AHR; ref. 43), a ligand-activated transcription factor able to induce cell proliferation (reviewed in ref. 44). Therefore, we examined whether SAA1 induces AHR-dependent transcription of classic target genes. Indeed, exposure of human AML and MDS cell lines to SAA1 upregulated most of the main AHR target genes (Supplementary Fig. S5J). Similar to what we observed with *IDO1* expression (Fig. 5E), *CYP1A1* and *CYP1A2* gene expression was upregulated only in response to SAA1 in the human BM cells isolated from the PDX AML but not in the cells isolated from $CD34^+$ healthy injected mice (Fig. 5I), confirming the specificity of this mechanism for leukemic cells. We further confirmed these results in BM-MNCs of patients, showing that both AHR target genes were specifically upregulated in samples from patients with AML but not from healthy subjects (Fig. 5J). Finally, we corroborated this AHR target gene activation pattern in the lineage-depleted AML and MDS BM-MNCs isolated from patient aspirates (Fig. 5K). Interestingly, an AHR activation signature was also upregulated in AML cells exposed to osteoblasts (Fig. 5L), and further confirmed in cocultures of leukemic cells with human osteoblasts, which showed upregulation of the *CYP1A1* and *CYP1A2* genes upon osteoblast exposure (Supplementary Fig. S5K). Altogether, these data suggest that SAA production by osteoblasts upregulates *IDO1* expression in AML cells through activation of the AHR pathway.

Pharmacologic Targeting of the Kyn–HTR1B–SAA–IDO1 Axis in Xenografts Impairs AML Proliferation

The demonstration that *IDO1* ablation has potent antileukemic effects prompted us to explore the therapeutic potential of inhibiting IDO1 activity for leukemia growth. Therefore, we analyzed the effect of epacadostat, a potent, selective, and competitive inhibitor of IDO1 enzymatic activity (45, 46), in leukemia progression. WT mice receiving epacadostat in an *ad libitum* diet (0.8 g/kg) showed a 54% reduction in their basal (no leukemia) circulating Kyn/Trp levels (Supplementary Fig. S6A) and, consistent with previous reports (47), did not show any obvious systemic toxicity. In the MLL/AF9 leukemic mice, we observed a slight—yet significant—increase in survival when mice were treated with epacadostat (Supplementary Fig. S6B). However, despite a tendency toward a slower leukemia progression (Supplementary Fig. S6C), the *in vivo* pharmacology of epacadostat at the selected dose was such that it did not reduce the 1.5-fold increase in systemic Kyn/Trp levels observed in the MLL/AF9 leukemic mice (Supplementary Fig. S6A). Doubling the epacadostat dose (1.6 g/kg) resulted in a 35% reduction in serum Kyn levels (Supplementary Fig. S6D), a significant delay in AML burden (Supplementary Fig. S6E), and a significantly prolonged survival as compared with the lower dose (Fig. 6A). Hence, reduction in Kyn levels proportionally affects leukemia burden and overall survival.

Subsequently, we investigated the effect of pharmacologic inhibition of the Kyn pathway in a clinically relevant PDX model of human AML. First, we verified that regulation of the Kyn–HTR1B–SAA axis is reproduced in response to AML in xenografts. Consistent with our observations in murine models and patient samples, immunodeficient (NSGS) mice transplanted with patient-derived human AML cells showed higher SAA3 (Fig. 6B) and Kyn/Trp ratio (Fig. 6C; Supplementary Fig. S6F) peripheral levels as compared with PDX mice transplanted with $CD34^+$ healthy cells. Moreover, mirroring our observations in patient samples (Fig. 4I), we observed a positive correlation between both biomarkers and disease state (Supplementary Fig. S6G). These results not only demonstrate the conserved response and activation of this axis in mammals, but also reinforce the notion of assessment of both Kyn and SAA1 as biomarkers in the diagnosis of AML progression.

Patient-derived *de novo* AML cells were injected into sublethally irradiated NSGS mice (Fig. 6D), and three weeks after transplantation, BM aspiration was performed to randomize the groups (Supplementary Fig. S6H). To control the daily intake of epacadostat, we opted for a 12-day regimen of daily gavage (300 mg/kg). While achieving only a ~20% reduction in Kyn/Trp levels in blood (Fig. 6E; Supplementary Fig. S6I)—likely owing to the short duration of the treatment—epacadostat-treated animals showed a concomitant ~20% reduction in AML BM burden compared with the vehicle-treated group (Fig. 6F). Moreover, *in vivo* assessment of the leukemic blast ($hCD45^+CD33^+$) cell cycle showed that epacadostat-treated leukemic blasts were less proliferative than the vehicle-treated ones (Fig. 6G). Interestingly, although the G_0–G_1 and G_2–M populations remained

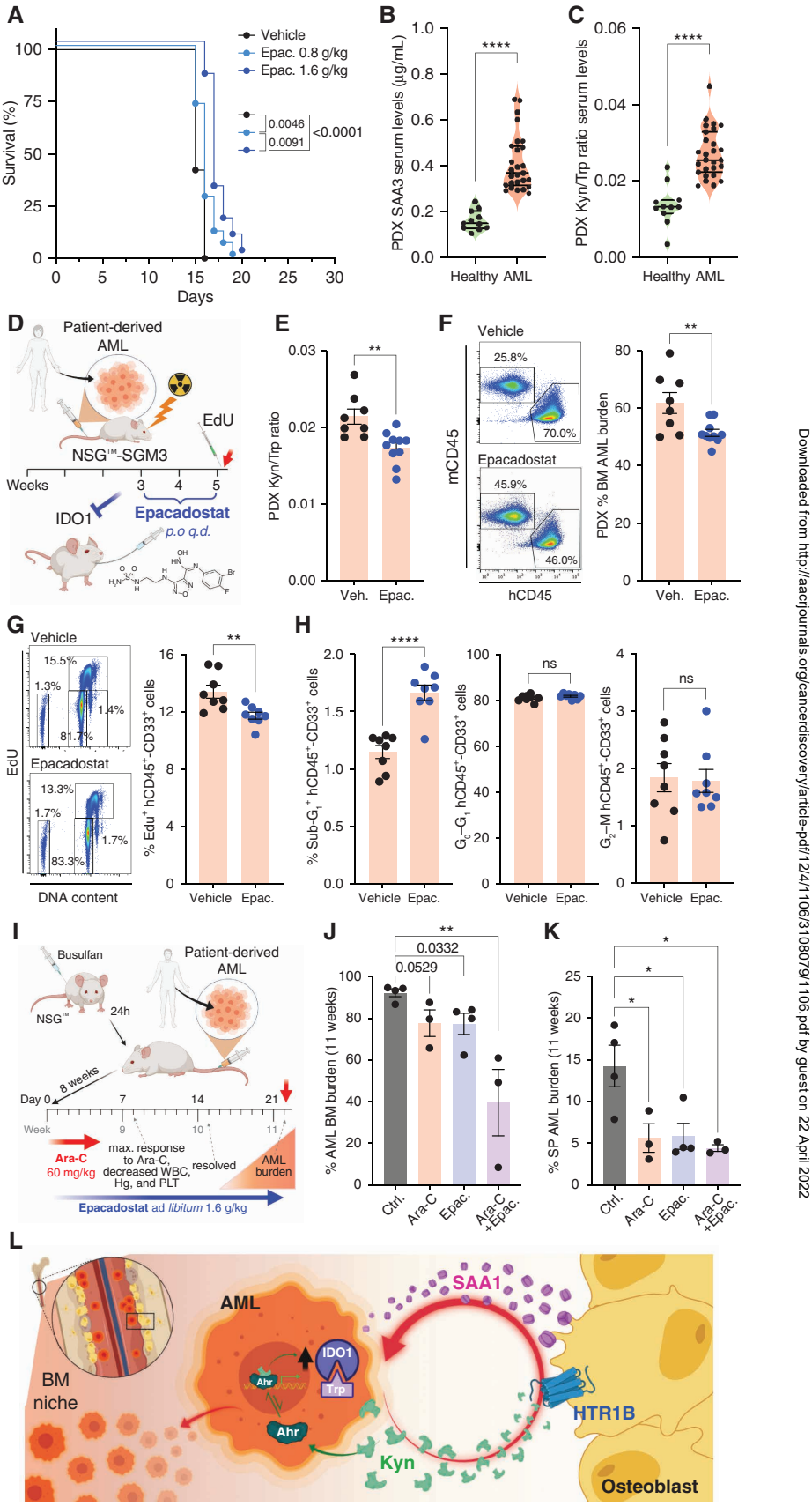

Figure 6. Pharmacologic targeting of the Kyn–HTR1B–SAA–IDO1 axis in PDXs. **A,** Survival curve comparing vehicle ($n = 26$) and epacadostat-treated mice ($n = 18$ for 0.8 g/kg and $n = 13$ for 1.6 g/kg). Kaplan–Meier curve with *P* value of log-rank (Mantel–Cox) test. SAA3 (**B**) and Kyn/tryptophan (Trp) ratio (**C**) serum levels in NSGS mice transplanted with CD34$^+$ healthy cells ($n = 11$) or with patient-derived AML cells ($n = 27$). **D,** Schematic describing pharmacologic targeting of IDO1 (epacadostat) in patient-derived AML xenograft (PDX) in NSGS mice. **E,** Kyn/Trp ratio in serum of PDX mice 5 weeks after AML transplant and 2 weeks after epacadostat treatment ($n = 8$ vehicle; $n = 10$ epacadostat). **F,** Representative flow cytometry plots depicting the percentage of human or mouse CD45$^+$ cells in the BM of PDX mice (left) and AML burden in the BM of PDX mice at harvest (right; $n = 8$ vehicle; $n = 10$ epacadostat). **G,** Representative flow cytometry plots (left) and cell-cycle analysis of leukemic blasts (CD45$^+$ CD33$^+$) of PDX mice treated with either vehicle ($n = 8$) or epacadostat (Epac; $n = 8$). **H,** Cell-cycle analysis of mice in **G**. **I,** Schematic diagram showing the *in vivo* PDX mouse model treated with the combination therapy (Ara-C 60 mg/kg 1–5 days + epacadostat 1.6 g/kg *ad libitum* 3 weeks). AML burden in BM (**J**) and SP (**K**) 11 weeks after transplant, three weeks after combination therapy; control chow (ctrl; $n = 4$), Ara-C ($n = 3$), epacadostat ($n = 4$), and combination therapy (Ara-C + epacadostat, $n = 3$); one-way ANOVA; unpaired *t* test *P* values are shown for BM ctrl versus Ara-C and epacadostat groups. **L,** Schematic model of the Kyn–HTR1B–SAA–IDO1 axis depicting the AML-mediated osteoblastic self-reinforcing niche remodeling. All data expressed as mean ± SEM. Statistical analysis done with unpaired *t* test unless otherwise stated. *, $P \le 0.05$; **, $P \le 0.01$; ****, $P \le 0.0001$. See also Supplementary Fig. S6. Hg, hemoglobin; PLT, platelets.

unchanged, epacadostat treatment increased leukemic blast apoptosis (Fig. 6H), contrary to the antiapoptotic effects observed upon SAA1 treatment (Supplementary Fig S5D).

Finally, we explored the therapeutic potential of targeting the Kyn–HTR1B–SAA–IDO1 axis in an established PDX leukemia model by inhibiting Kyn synthesis as an adjuvant treatment for chemotherapy (Fig. 6I). Eight weeks after transplant, at the time of randomization, BM aspiration showed ~50% AML burden (Supplementary Fig. S6J). Leukemic mice were then treated for three weeks with control chow, chemotherapy alone [1-β-D-arabinofuranosylcytosine (Ara-C) for five days; ref. 48], epacadostat diet (*ad libitum*, 1.6 g/kg), or combination therapy (Ara-C + epacadostat). As previously described in this model (48), leukemic burden is decreased by day 8 after initiating therapy with single-agent Ara-C, but relapse occurs consistently between 22 and 29 days after starting therapy (Fig. 6I). As expected with assessment at day 22, although not significant (probably due to the low number of mice), Ara-C alone–treated mice had a modest decrease in overall leukemic burden, likely indicating that relapse is under way (Fig. 6J). The effect of Ara-C was more sustained in the SP than in BM, in agreement with previous results in this model (48, 49). Consistent with above results (Fig. 6F), epacadostat as a standalone intervention also decreased leukemic burden in the BM of NSG mice (Fig. 6J; Supplementary Fig. S6K), and as with Ara-C, it had a more pronounced effect in the SP (Fig. 6K). Importantly, we assessed the effect of epacadostat/Ara-C combination at day 22 after initiating therapy. The combination treatment significantly decreased leukemic burden in the BM and SP, although this effect was synergistic only in the BM (Fig. 6J and K). Thus, epacadostat inhibition of IDO1 enhances the response to Ara-C in this preclinical model.

Collectively, our results reveal that leukemia cells subvert serotonin signaling in osteoblasts, inducing a self-perpetuating proinflammatory niche by exploiting the Kyn–HTR1B–SAA–IDO1 axis (Fig. 6L). These results provide strong evidence for a central role of the Kyn–HTR1B–SAA–IDO1 axis in human AML progression. Moreover, they provide proof of principle that targeting this axis can be therapeutically beneficial in ways that complement standard induction therapies and described immunosuppressive effects of Kyn.

DISCUSSION

This study identifies a new mechanism underlying AML progression with the potential to affect the management of myeloid malignancies. We show that AML cells seize a peripheral serotonin signaling pathway to instruct a cycle of feedback signals in niche osteoblasts promoting leukemia proliferation (Fig. 6L). This is achieved through the preferential production of Kyn by AML cells, which in this setting acts as an oncometabolite and a previously unrecognized ligand of HTR1B. AML niche remodeling induces a proinflammatory signature in osteoblasts. Among the several proinflammatory molecules, the expression of which is upregulated in osteoblasts, leukemia-secreted Kyn specifically induces SAA expression through HTR1B. In turn, osteoblast-secreted SAA acts in AML cells to upregulate *IDO1* expression, self-reinforcing leukemia proliferation. SAA1-dependent *IDO1* upregulation promotes AML progression in a cell-intrinsic manner by increasing Kyn secretion (and thus activating the AHR pathway, which enhances leukemia cell proliferation), as well as by facilitating tolerance and immune escape (reviewed in ref. 50). Highlighting the clinical relevance of these findings, preferential production of Kyn over serotonin by leukemic cells, as well as increased levels of SAA1 in the BM plasma, marks disease progression in MDS to AML patients, suggesting their potential use as biomarkers of disease progression.

In our previous study, we showed that osteoblast ablation increases leukemia burden, whereas maintaining osteoblast numbers reduces leukemia (19). At the same time, we described a decrease in osteoblast numbers in patients with AML and mouse models, and indeed we show here that AML cells induce a proapoptotic signature in osteoblasts. Additionally, in the current study we show that disruption of a specific pathway elicited by leukemia cells in osteoblasts in fact favors AML growth. We believe that these seemingly contradictory results indicate that osteoblasts perform a dual function: They exert protective signals and at the same time—instructed by the AML cells through the Kyn–HTR1B–SAA–IDO1 axis—favor leukemia growth. A balance between those two effects allows a steady leukemia growth that eventually leads to lethality. Decreasing osteoblast numbers disrupts this balance by reducing the protective signal while the Kyn–HTR1B–SAA–IDO1 pathway is maintained and able to outweigh the weakened protective effect faster, favoring AML growth. Further work is needed to identify the protective mechanisms elicited by osteoblasts and to clarify their role versus the role of peripheral serotonin signaling during disease growth.

HTR1B has previously been proposed to promote AML growth (51, 52) through its expression on AML cells, mainly based on the observation that pharmacologic inhibition of HTR1B improves disease outcome *in vivo*. This work, however, did not differentiate or directly assess the possibility that HTR1B signaling in BM stromal—not AML—cells may contribute to these actions. Nevertheless, our study reveals a distinct role of HTR1B in osteoblasts, activated by a previously unrecognized ligand of this receptor (Kyn), to stimulate the expression of a new AML-inducing player that we identify as SAA.

We show that Kyn levels mark disease in patients with MDS and AML. The importance of Trp catabolism in leukemia cells is supported by other studies showing that serotonin levels are drastically decreased in patients with MDS and AML as well as in leukemic mice (53), and that Kyn/Trp ratios associate with several malignancies, including AML (54–58). However, whether Kyn was a biomarker or an active determinant of disease progression was not known. Our study unveils oncometabolite properties of Kyn in MDS and AML. In addition, it reveals Kyn as a previously unappreciated ligand of HTR1B that seizes serotonin signaling in osteoblasts under leukemia instruction to implement a distinct function: remodel the osteoblastic niche to allow leukemia cell engraftment and progression. Indeed, in the absence of IDO1 in leukemia cells, the disease eventually fails to engraft and progress.

We also assign a new function of Kyn in cancer regulation that is distinct from its established involvement in enhancing cancer cell motility and immune escape. In these roles, Kyn acts via the AHR to favor tolerance and immune escape by activating T regulatory cells and myeloid-derived suppressor cells, as well as by suppressing the function of effector T cells and

natural killer (NK) cells (59–63). Herein we show that in MDS and AML, in addition to this immunomodulatory role, Kyn produced by malignant cells engages HTR1B in osteoblasts to promote secretion of SAA, which in turn, acting through the AHR, amplifies and maintains leukemia growth by upregulating *IDO1* expression. We demonstrate that this particular Kyn–HTR1B–SAA–IDO1 axis is required to maintain disease progression. Kyn may also confer immunomodulatory advantages to MDS and AML cells (54–58). In this instance, the osteoblast-centric HTR1B–SAA axis may be a means for MDS or AML cells to both favor their proliferation and, at the same time, suppress the immune response to escape immunosurveillance by amplifying their production of Kyn.

The identification of the Kyn–HTR1B–SAA–IDO1 axis in promoting AML growth may be relevant to other cancers and could be exploited in combination with immunotherapy to overcome current challenges. Indeed, based on the immunomodulatory profile of Kyn–AHR signaling in cancers, small-molecule inhibitors of IDO1 have entered clinical trials as an adjunct to immune-checkpoint blockade to concomitantly target these two immunosuppressive mechanisms (64, 65). However, the first phase III clinical trial failed (66) and, as a result, several ongoing phase III clinical trials testing epacadostat, alone or in combinatorial regimen in different cancer contexts, were downsized or suspended. Nevertheless, in the only completed phase III trial, Kyn levels were not measured to assess the effectiveness of IDO1 inhibition, and there was a lack of patient stratification based on IDO1 expression. Although IDO1 inhibitors (like epacadostat) may have negligible effects on established cancers—or in MDS itself (67)—as single agents, the combination of targeting the Kyn–HTR1B–SAA–IDO1 axis along with current immunotherapies—including immune-checkpoint blockers—could yield a synergistic effect to block disease progression, favoring survival. Indeed, the use of immunocompromised mice (lacking mature B, T, and NK cells, circulating complement, as well as showing defective dendritic cells and macrophages) highlighted the therapeutic effects of targeting IDO1 by acting directly on leukemic blasts, as responses from the host immune system were unlikely in the immunocompromised setting.

AML, a highly lethal hematologic malignancy, is characterized by the clonal expansion of immature myeloid blasts in the BM and/or peripheral blood. This hematopoietic cancer, prevalent in the elderly, remains recalcitrant to treatment, particularly because residual clones persist through therapy and ultimately cause relapse. As a result, and despite improvements in diagnosis and treatment-adapted regimens, targeted therapies have not achieved desired remissions, clinical management of AML has barely changed for the last half century (68), and overall survival rates remain low (five-year survival rate less than 30%; refs. 68, 69). These shortcomings highlight the urgency of proposing novel and adapted therapies for the disease.

The ultimate goal of research into the niche of hematologic malignancies is the development of therapies targeting the BM microenvironment alone or in combination with existing therapies. This can be accomplished by targeting interactions between malignant cells and their niche, or malignant hematopoietic cell-intrinsic pathways that directly influence the BM microenvironment. Relevant approaches within this concept hold such promise (70–73), yet targeting the niche as an adjunct therapy is only starting to be developed. Our observations that genetic and pharmacologic inhibition of the Kyn–HTR1B cross-talk taking place between leukemia cells and osteoblasts hampers AML engraftment suggest that disrupting this interaction, alone or in combination with existing therapies, may be a new and adapted therapeutic approach for AML. In a proof-of-concept experiment, chemotherapy combined with the IDO1-specific inhibitor epacadostat proves to be effective in addressing the recurrent relapse observed in patients with AML after chemotherapy treatment. The independence of such a niche-focused approach from cell-intrinsic genetic or epigenetic defects in malignant cells underscores its therapeutic value to overcome the recalcitrance arising from clonal evolution and the emergence of therapy-resistant clones, and, as a result, to promote durable remission in patients with AML.

METHODS

Mice

WT C57BL/6J (IMSR, catalog no. JAX:000664, RRID:IMSR_JAX:000664), BALB/cJ (IMSR, catalog no. JAX:000651, RRID:IMSR_JAX:000651), NSG (IMSR, catalog no. JAX:005557, RRID:IMSR_JAX:005557), and NSGS (IMSR, catalog no. JAX:013062, RRID: IMSR_JAX:013062) mice were purchased from Jackson Laboratories. All other animals used in the study were bred in our mouse facility, kept in a C57BL/6J background and used between 8 and 10 weeks old. Male and female mice were used indiscriminately. *Htr1b*$^{-/-}$ mice were obtained from Dr. Rene Hen at Columbia University (30). *Htr1b*$^{fl/fl}$ mice were obtained from Dr. Greengard at Rockefeller University (74) and were mated to LepR-Cre, COL1A-Cre (33), OCN-Cre (34), or Osx-Cre (35) to generate homozygous mice lacking *Htr1b* in the indicated tissues. The Osx-Cre mice were kept on doxycycline-containing diet (0.625 g/kg); doxycycline was removed in the experimental group 24 hours after MLL/AF9 injection. All mouse genetic models were used with their respective WT littermates as controls. Experimental animals have been maintained at the Columbia University animal facility under specific pathogen-free conditions and in accordance with Institutional Animal Care and Use Committee of Columbia University approved protocols.

PTH Bone-Anabolic Treatment. Mice were injected intraperitoneally (i.p.) with PTH (Bachem) at 80 μg/kg/day in PBS. Injections started 1 week before MLL/AF9 injection and continued along two to three more weeks until mice were harvested.

SB224289 (SB9) Treatment. Mice were injected i.p. daily with SB9 (5 mg/kg in 0.9% NaCl) 1 week after leukemia injection and for the duration of the experiment. Assuming a 20 g body weight (BW) and a 2 mL total blood volume per mouse—as well as an even distribution of the drug—systemic concentration of SB9 (TOCRIS, catalog no. 1221) should be approximately 50 μg/mL. Based on the molecular weight of SB9 (557.09), the final concentration—at equal distribution—in blood should be 8.97521e^{-05} mol/L (≈90 μmol/L).

Epacadostat Treatment. For the WT C57BL/6J mice, treatment started at the same time when MLL/AF9 cells were transplanted. For the patient-derived AML cells (PDX) transplanted into NSG mice, treatment started eight weeks after transplant, at the same time as Ara-C and during three weeks. Mice were supplied with *ad libitum* epacadostat (AdooQ, catalog no. A15554)-supplemented diet (Research Diets Inc.) at 800 mg/kg (low dose) or 1.6 g/kg (high dose). For the PDX transplanted into NSGS mice, treatment started three weeks after transplant, by daily gavage at 300 mg/kg

(InvivoChem, catalog no. V0942, dissolved in 10% DMSO, 40% PEG 300, and 50% NaCl 0.9%) for two weeks.

SAA1 Treatment. For short-term treatment (two days), mice were injected i.v. 72 and 48 hours before harvesting. For long-term treatment (eight days), mice received daily i.v. injections. In order to get the same SAA1 concentration in blood that was used *in vitro*, we used a dosage of 100 μg/kg of SAA1 (PeproTech, catalog no. 300-53), diluted in 0.9% NaCl. Assuming a 20 g BW, 2 mL total blood volume, and an even distribution in the mouse, systemic concentration of SAA1 should be approximately 1 μg/mL.

Serum for ELISA Analysis. Serum for ELISA analysis was collected from cardiac puncture, left untouched for 30 minutes at room temperature, and centrifuged 15 minutes at 4°C 12.000 rpm; samples were snap-frozen in liquid nitrogen and stored at −80°C until further analysis.

Complete Blood Counts. Complete blood counts were assessed on cardiac-puncture peripheral blood (at harvest/endpoint) collected into EDTA-coated tubes (Becton Dickinson) using a Genesis (Oxford Science) hematology system.

Patient Samples

Primary MDS and AML Patient Samples. BM aspirate samples and bone biopsies from male and female patients with MDS and AML between the ages of 53 and 87 were obtained from an Institutional Review Board (IRB)–approved tissue repository at the Myelodysplastic Syndromes Center at New York Presbyterian–Columbia University Medical Center. Three to 10 mL of BM aspirate was collected from the iliac crest of the back of the hip bone. 0.5–1 mL was used for BM plasma collection (15 minutes at 2,000 × *g* 4°C), snap-frozen in liquid nitrogen, and stored at −80°C until analysis. The study populations reflected the populations usually seen at the clinics at Columbia University Medical Center. Those include 60% males and 40% females, with 60% Caucasian, 30% Hispanic, and 10% African American and non-Hispanic. MDS and AML are predominantly a disease of the elderly (median age at diagnosis, 74 years). Fewer than 15% of the patients with MDS are between the ages of 18 and 65 and greater than 85% will be above age 65.

BM samples from the University of Pennsylvania were obtained from the Stem Cell and Xenograft Core. The core has maintained an IRB-approved protocol for 20 years. All samples were obtained as deidentified and previously collected. As with Columbia University Medical Center, the race and sex of samples in the core reflect those of the patient population seen at the Hospital of the University of Pennsylvania.

Healthy Biopsies. Healthy BM aspirates and bone biopsies were obtained from the Orthopedic Surgery Department at Columbia University, in collaboration with Dr. R. Shah. Healthy patients who had a planned elective hip or knee surgery were asked about their participation in the study, reflecting surgeries of men (44%) or women (56%) with ages ranging between 18 to 65 years old (46%) and >65 (54%).

All studies were approved by the Columbia University Medical Center IRB (Protocol Numbers AAAK3058 and AAAR3184), and informed written consent was obtained from all participants. Research was conducted in compliance with the declaration of Helsinki for collection and use of sample materials in research protocols, and in compliance with IRB regulations. Information on the primary human samples used in this study is described in Supplementary Table S1.

Isolation of BM-MNCs. Isolation of BM-MNCs was performed by density gradient centrifugation using Ficoll–Paque standard procedures.

Cell Lines and Primary Cell Cultures

OCI-AML3 (DSMZ, catalog no. ACC-582, RRID: CVCL_1844), THP-1 (DSMZ, catalog no. ACC-16, RRID: CVCL_0006), and MOLM-14 (DSMZ, catalog no. ACC-777, RRID: CVCL_7916) cells were acquired from the DSMZ repository. SC (ATCC, catalog no. CRL-9855, RRID: CVCL_6444), HL-60 (ATCC, catalog no. CCL-240, RRID: CVCL_0002), MV4-11 (ATCC, catalog no. CRL-9591, RRID: CVCL_0064), KG-1a (ATCC, catalog no. CCL-246.1, RRID: CVCL_1824), Kasumi-1 (ATCC, catalog no. CRL-2724, RRID: CVCL_0589), and HEK293T (ATCC, catalog no. CRL-3216, RRID: CVCL_0063) cells were obtained from the ATCC and WEHI-3B (ECACC, catalog no. 86013003, RRID: CVCL_2239) from Sigma. The MDS-L cell line was a kind gift from Dr. Amit K. Verma (Albert Einstein College of Medicine). Cell lines not directly obtained from their source were validated via short tandem repeat DNA profiling. All cell lines were routinely tested for *Mycoplasma* (Venor GeM Mycoplasma Detection Kit, Sigma-Aldrich, catalog no. MP0025).

OCI-AML3 and THP-1 cell lines as well as primary human osteoblasts were grown in MEM-Alpha 1× (Corning); HEK293T cells were grown in DMEM (Corning); SC, HL-60, MOLM-14, KG-1a, Kasumi-1, and MV4-11 cells were grown in Iscove's Modified Dulbecco's Medium (Gibco). The MDS-L cell line was grown in RPMI supplemented with 1× beta-mercaptoethanol and IL3 (10 μg/mL). All media were supplemented with 10% FBS (Gibco), except primary human osteoblasts OCI-AML3 and HL-60 that needed 20%, 1% GlutaMAX (Gibco), and 1% antibiotic-antimycotic (Corning), and cultured at 37 °C with 5% CO_2.

MLL/AF9 Primary Cells. MLL/AF9 primary cells were maintained in StemSpan medium (STEMCELL Technologies) containing mGM-CSF (10 ng/mL), mSCF (25 ng/mL), mIL6 (25 ng/mL), mIL3 (10 ng/mL), mTPO (25 ng/mL; PeproTech), and 1% penicillin/streptomycin (PS).

Human Primary MDS and/or AML Cells. Patient-derived AML cells for CRISPR experiments were cultured with Stemspan II (STEMCELL Technologies), 1% PS, completed with 100 ng/mL of human FLT3L and SCF, 50 ng/mL of human TPO, IL3, and IL6 (BioLegend), and 750 nmol/L of SR1 (Cayman Chemical). For the *ex vivo* cultures, AML and/or MDS cells were cultured on StemMACS HSC Expansion Media XF supplemented with StemMACS HSC Expansion Cocktail (Miltenyi Biotec).

Primary Human Osteoblasts. Primary human osteoblasts were obtained from explants of healthy patients undergoing hip/knee replacement surgery. Outgrowth cultures yielded osteoblastic stromal cells that were differentiated in osteogenic media (5 mmol/L β-glycerol phosphate and 100 μg/mL ascorbic acid; Sigma) changed every other day for 10 to 13 days.

Primary Calvaria-Derived Osteoblasts. Primary calvaria-derived osteoblasts were prepared from calvaria of two- to three-day-old newborns as previously described (75). Briefly, mice calvaria were sequentially digested for 20, 40, and 90 minutes at 37°C in α–minimum essential medium (α-MEM; Gibco) 10% FBS containing 0.1 mg/mL of collagenase P (Worthington) and 0.25% trypsin (Gibco). Cells of the first two digests were discarded, whereas cells released from the third digestion were plated and differentiated for 7 to 10 days as previously described.

Cocultures. Cocultures were set up using a 0.4-μm-pore transwell (Falcon), with primary osteoblasts on the bottom compartment and the leukemic cells on the top one. Both cells were starved overnight and cocultured together in α-MEM for the indicated period of time in an osteoblast-to-leukemia ratio of 1:10.

Treatments with Recombinant Proteins. Human IL1α, IL1β, IL6, IL33, IL34, CXCL1, CXCL3, CXCL5, CXCL8, CCL2, CCL20, Apo-SAA1 (all from PeproTech), and recombinant mouse SAA3 (Cusabio) were treated overnight with 50 ng/mL of the corresponding protein. SAA1 treatment of human AML cell lines was done with 1 μg/mL for 24, 48, or 72 hours. Treatment of primary human MDS or AML lineage–depleted BM-MNCs was done with 5 μg/mL for 24 hours. Treatment of PDX isolated human total BM cells was done with 1 μg/mL for 24 hours.

Leukemic Syngeneic Mouse Models and Assessment of Leukemia In Vivo Progression

All leukemia models were introduced by i.v. injection and transplanted into nonirradiated secondary recipient experimental animals. BALB/c mice were used for the WEHI-3B leukemia model (0.5×10^6/cells/mouse) and C57BL/6J mice for MLL/AF9-dsRed (0.2×10^6/cells/mouse). Leukemia progression was assessed by fluorescence (MLL/AF9 dsRed) using the IVIS-Spectrum Optical Imaging System (Caliper, PerkinElmer). Mice were shaved to reduce light attenuation.

Xenograft Models

Four- to six-week-old NSG (cell line–derived xeonograft model) or NSGS (PDX model) mice were preconditioned with sublethal (1.4 Gy) total-body irradiation. After 24 hours, 1×10^6 OCI-AML3 or 2×10^5 human BM CD34$^+$ (healthy) or primary AML patient samples were injected i.v. Engraftment levels were monitored, and mice were randomized after BM aspiration three to four weeks later and immunophenotyped by the presence of mCD45 (BioLegend, catalog no. 103133, RRID:AB_10899570), hCD45 (BioLegend, catalog no. 368512, RRID: AB_2566372), hCD33 (BioLegend, catalog no. 303404, RRID: AB_314348), hCD34 (BioLegend, catalog no. 343518, RRID: AB_1937203) cell populations. For the low-burden PDX model (Kyn injections), mice were treated one week after transplant.

Combination Therapy (Chemotherapy ± Epacadostat). For the combination therapy (chemotherapy ± epacadostat) performed at the University of Pennsylvania, patient-derived AML cells were transplanted as previously reported (48). Briefly, six-week-old NSG males were sublethally treated with busulfan (30 mg/kg) 24 hours before transplant, and 5×10^6 patient-derived AML cells were injected i.v. Engraftment was assessed and mice were randomized at 7.5 weeks by BM aspirate as previously described. Randomized mice were treated with vehicle, Ara-C (60 mg/kg/day × 5 days i.p.), epacadostat chow (1.6 g/kg *ad libitum*), or both Ara-C and epacadostat chow for three weeks.

Immunofluorescence Staining

Tissue. After harvesting, SP and liver were fixed overnight in 4% paraformaldehyde (PFA), washed with PBS, and kept on a 30% sucrose gradient for at least 16 hours before OCT. For bones, fixation was done for 72 hours following 7 days of decalcification on 14% EDTA pH7 before sucrose gradient and OCT embedding. All tissues were cut using a Leyca cryostat, dried at room temperature, and stored at −80°C. Sections were rehydrated in PBS for 10 minutes and stained with DAPI.

Cells. Osteoblasts were grown over 12-mm coverslips, differentiated, and exposed for 30 to 60 minutes to conditioned media from OCI-AML3 cells at a 1:10 ratio, fixed in 4% PFA 15 minutes at room temperature, permeabilized (PBS 0.3% Triton X-100) 15 minutes at room temperature, blocked (PBS 5% donkey normal serum, 0.3% Triton X-100), and stained overnight at 4°C with p65 (Cell Signaling Technology, catalog no. 8242, RRID:AB_10859369) and DAPI (nuclei). Slides were mounted with Antifade Prolong Gold (Invitrogen) mounting medium, and images acquired on a Zeiss LSM 710 confocal microscope. Images were analyzed with ImageJ (RRID:SCR_003070) software.

Metabolomics

Cell culture supernatant samples (150 μL) were loaded into Ostro Protein Precipitation and Phospholipid Removal Plate (Waters: 186005518). Twenty microliters of internal standards and 450 μL of acetonitrile (0.2% formic acid) were added. After pressure pushing through the plate, the samples were transferred to a new vial and dried under gentle nitrogen flow. The samples were reconstituted to 100 μL of 80% methanol–20% water for analysis with ABsciex 6500+ with Ace PFP column. A pooled quality control sample was injected ×6 for CV calculation. Metabolites with CVs < 20% are considered as accurate quantification, whereas CVs > 35% are treated as poorly accurate results. Principal component analysis (PCA) 2D scores plot was calculated to show the degree of overlap between the three data point clusters in principal component (PC) scores space. The partial least squares-discriminant analysis (PLS-DA) scores plot was calculated with PC1 representing the difference between the three groups and PC2 differences between the cocultures and the AML. Analysis of metabolomic data was performed on Matplotlib for Python.

LC/MS

Cell culture supernatant samples were analyzed at the Biomarkers Core Laboratory (BCL) of Columbia University by targeted LC/MS-based assays for the biogenic amines Trp, Kyn, and serotonin.

Kyn, Trp, SAA3, and SAA1 Serum/Plasma Levels

Quantification in serum from peripheral blood (mice) or BM plasma (patients) of Kyn and Trp was assessed by ELISA using independent kits (ImmunoSmol) as per the manufacturer's instructions. The ratio between Kyn and Trp levels is shown. SAA3 in serum (murine SAA3 ELISA Kit Millipore) and SAA1 in patient BM plasma (Amyloid A1 DuoSet ELISA Kit, R&D Systems) were assessed as per the manufacturer's instructions.

Total RNA Extraction and RT-qPCR Gene Expression Analysis

RNA isolation, cDNA preparation, and real-time PCR analyses were carried out following standard protocols. Total RNA from cortical bone (clean, flushed femurs, centrifugated 20 seconds at $10.000 \times g$ to remove any remaining BM) was extracted using TRIzol (Invitrogen) followed by RNA clean-up using the PureLink RNA Mini Kit (Ambion, Invitrogen). mRNA was reverse-transcribed using random hexamers RNA-to-cDNA kit (Takara). Specific forward and reverse primers were used in conjunction with PowerUp SYBR Green Master Mix (Applied Biosystems) for quantitative PCR. Expression levels were analyzed using the $2^{-\Delta\Delta Ct}$ method and were normalized for the expression of the housekeeping gene *Hprt* unless otherwise stated.

Radioligand Binding Assays

The full-length murine or *Htr1b* (pCMV6-Entry vector, Myc-DDK-tagged, Origene, catalog no. MR222524 and RC223874, respectively) were transiently transfected into HEK293T cells using Lipofectamine LTX (Invitrogen). Transfection efficiency was assessed 24 hours after transfection by flow cytometry using the anti-FLAG antibody (Sigma-Aldrich, catalog no. F3165, RRID:AB_259529). Binding of 25 nmol/L [^{3}H]-5-HT (41.3 Ci/mmol, PerkinElmer) or [^{3}H]-Kyn (50 μmol/L, 0.125 Ci/mmol) was performed with 100 μg of isolated HEK293 membranes in a final volume of 50 μL of binding buffer (10 mmol/L HEPES, pH 7.4, 100 mmol/L NaCl, 10 mmol/L $MgCl_2$, 1% ascorbic acid, 1× entacapone/pargyline), incubated for 3 hours at 4°C in the presence of varying concentrations of nonlabeled additions (5-HT,

Kyn, or SB9). Reactions were stopped by the addition of ice-cold PBS, filtered through 0.7-μm glass fiber filters (Data Support Company). Filters were dried and melted with scintillation cocktail. Radioactivity captured on the filters was counted using an SL300 scintillation counter (Hidex). Unspecific binding of [^{3}H]-5-HT or [^{3}H]-Kyn in the presence or absence of each compound with the glass filters was determined in the absence of membranes; specific binding was determined by subtracting the unspecific binding signal from that measured in the presence of the HTR1B-expressing membranes in the appropriate conditions. LogEC_{50} were determined by nonlinear regression curve analysis.

[^{3}H]-GR125743 Radioligand Binding Assay. [^{3}H]-GR125743 (PerkinElmer) radioligand binding assays were performed in standard binding buffer (50 mmol/L Tris, 10 mmol/L $MgCl_2$, 0.1 mmol/L EDTA, 0.1% BSA, 0.01% ascorbic acid, pH 7.4). Competitive binding was assessed with various concentrations of test compounds (0.3 nmol/L to 100 μmol/L), [^{3}H]-GR125743 (1.38 nmol/L), and *HTR1B* membranes (isolated from HEK293T stable transfectants) in a total volume of 150 μL. Assay plates were incubated in the dark for one hour at room temperature, and reactions were stopped by filtration onto 0.3% polyethyleneimine presoaked 96-well Filtermat A (PerkinElmer), followed with three quick washes with cold wash buffer (50 mmol/L Tris, pH 7.4). Filters were dried and melted with scintillation cocktail (Meltilex, PerkinElmer). Radioactivity was counted using a Wallac TriLux Microbeta counter (PerkinElmer). The procedures and protocols of binding assays are also available online at https://pdsp.unc.edu/pdspweb/.

cAMP Signaling Assays

The GloSensor cAMP assays were conducted as previously reported (76) with minor modifications. Briefly, HEK293T cells were transiently cotransfected with 4 μg of 5-HT_{1B} receptor and 4 μg of GloSensor cAMP (Promega) plasmids overnight and plated in poly-L-lysine coated 384-well white clear-bottom plates in DMEM supplemented with 1% dialyzed FBS for 24 hours. Cells were removed from the culture medium and loaded with luciferin (final of 1 mmol/L) for 30 minutes at 37°C. The cells were then stimulated with the drugs diluted in assay buffer (HBSS, 20 mmol/L HEPES, 1 mg/mL BSA, pH 7.4) for 15 minutes at room temperature, followed by the addition of isoproterenol (100 nmol/L). The plates were counted in a Wallac TriLux Microbeta counter (PerkinElmer) after 25 minutes.

Proliferation Assays

Cell proliferation was performed by using Cell Counting Kit 8 (WST-8, Abcam) as per the manufacturer's instructions. Briefly, 0.03×10^6 cells were seeded on tissue-culture clear bottom microplates (Corning) in their corresponding media (100 μL). When indicated, cells were treated with the indicated compounds and for the indicated time points. 10 μL/well of WST-8 solution was added and incubated for 2 hours at 37°C before measuring absorbance at 460 nm. For each experiment, the absorbance of the blank wells (growth media and vehicle/treatment) was subtracted from the values for those wells with cells.

In Vitro. The indicated cell lines were incubated in reduced-serum media and exposed to SAA1 (1 μg/mL) for 24 to 72 hours as indicated.

Ex Vivo *Xenografts (Healthy CD34$^+$ versus Patient-Derived AML).* Total BM from NSGS mice was depleted of mouse cells with mouse CD45 magnetic beads (Miltenyi Biotec; catalog no. 130-052-301, RRID:AB_2877061) and negatively selected human cells were used.

Ex Vivo *Primary AML and MDS Patient Samples.* MNCs from fresh BM patient aspirates were isolated as previously described and depleted from mature hematopoietic cells (Lineage Cell Depletion Kit, Miltenyi Biotec, catalog no. 130-092-211). Isolated cells were seeded on StemMACS HSC Expansion Media XF supplemented with StemMACS HSC Expansion Cocktail (Miltenyi Biotec, catalog no. 130-100-463 and 130-100-843) and treated with either vehicle (PBS) or SAA1 (5 μg/mL) for 24 hours.

In Vivo *Proliferation (EdU) Cell-Cycle Analysis*

Cell labeling was done by i.p. injection of mice with 50 mg/kg of freshly prepared EdU (Cayman Chemical Company, catalog no. 20518). After three to four hours, BM was harvested, and human cells were negatively selected by mouse cell depletion using mouse CD45 magnetic beads (Miltenyi). The human BM cells were then stained with CD45 and CD33 to identify the leukemic blast. Cell-cycle/proliferation analysis was performed using the Click-iT Plus EdU Flow Cytometry Assay Kit (Invitrogen, catalog no. C10420) following the manufacturers' instructions. Fixable viability dye (BioLegend) was used to discriminate the death population. Single-color controls were used to set compensations, and fluorescence minus one control were used to set gates. Analysis was performed with FlowJo software.

CRISPR/Cas9-Mediated Ido1/IDO1 *Genomic Targeting*

The chemically modified sgRNAs targeting *Ido1*/*IDO1* were obtained and designed with at least three mismatches to decrease possible off-target effects with the Synthego CRISPR design tool or the CRISPOR. Analysis of the predicted coding protein genes for each sgRNA did not reveal enrichment for any specific pathway or cellular process, especially no gene signature associated with p53 or DNA-damage pathways were identified (Supplementary Table S2). In addition, a lack of random effects due to p53 activation was shown by p16 and p21 mRNA level assessment in Cas9-only controls as well as in all the sgRNAs used (Supplementary Item S1). For 10^6 cells, 3 μg of TrueCut Cas9 protein V2 (Invitrogen) and 1.5 μg sgRNA was mixed in either SE (immortalized cell lines WEHI-3B and OCI-AML3) or P3 (primary mouse MLL/AF9 or patient-derived AML cells) buffer (Lonza, Amaxa X-Nucleofector Kit) and incubated 10 minutes. Cells were then resuspended in their respective nucleofection buffer, mixed with the Cas9/sgRNA RNP complex or the Cas9 only as control, and electroporated with the Lonza 4D-Nucleofector (program DZ100, CM137, or DI100). After electroporation, cells were cultured in their respective media at 37°C until sequencing analysis and/or injection. The editing efficiency data, indel contribution, and Sanger sequence analyses were performed with the Synthego Performance Analysis, ICE Analysis, 2019, v2.0 (Synthego).

Plasmid Constructs and Lentiviral Transduction

Lentiviral particles were obtained by cotransfection of Lenti-X Packaging Single Shots (VSV-G; Takara Bio, catalog no. 631275) and either empty or pLenti-IDO1-C-mGFP Vector (Origene, catalog no. RC206592L2) in HEK293T cells, according to the manufacturer's protocol. Supernatants containing the viral particles were concentrated using PEG Virus Precipitation Kit (BioVision, catalog no. K904) according to the manufacturer's protocol. Viral titers were quantified using Lenti-X GoStix Plus (Takara Bio, catalog no. 631280). 2×10^6 OCI-AML3 cells were transduced with the indicated multiplicity of infection by spinoculation ($300 \times g$ for one hour at 32°C) in the presence of 8 μg/mL polybrene (Millipore) 24 hours before assessment of proliferation.

RNA-seq

Briefly, total RNA was extracted from primary human osteoblasts and THP-1 cells cocultured with the transwell device using TRIzol. Paired-end transcriptome reads were processed using STAR (77) aligner based on the Ensembl (RRID:SCR_002344) GRCh37 human

genome assembly with default parameters. Read count values were extracted using featureCounts (78), and normalized gene expression was calculated as TPM. Differential expression analysis was performed with DESeq2 (RRID:SCR_015687; ref. 79). The RNA-seq data are deposited in Gene Expression Omnibus (GEO; GSE154374).

Multiplex Analysis of Protein Levels

Cell culture supernatants were probed for IL1α, IL6, CXCL1, CXCL5, CXCL8, CCL2, CCL7, CCL8, and CCL20 using a custom-made multiplex panel (Invitrogen ProcartaPlex) per the manufacturer's instructions. Supernatant samples were clarified by centrifugation at 10,000 × *g* for 10 minutes and kept on ice before loading.

Statistical Analysis

Sample size determination for *in vivo* experiments was estimated by considering a multifactorial variance analysis; a minimum number of mice ($n = 5$) assigned to each treatment group would reach a power of 0.85. The type I error probability associated with our tests of the null hypothesis was 0.05. Samples and mice were assigned to the different experimental groups in a random fashion. Male and female mice were used. Investigators were unblinded. Blinding during animal experiments was not possible because mice underwent a specific leukemia injection diet supply and/or daily treatment. No data were excluded from the study. We confirm that all experiments were reproducible by repeating them a minimum of two times—generally three to four times—using different stocks of cell lines, patient or mouse samples, and reagents. All single data points in all the figures represent biological replicates, from separate mice, separate experiments (cell lines), or, in the case of primary cultures of human or murine osteoblasts, measurements were performed on independently grown cultures. In the case of human data, each data point corresponds to an independent patient sample. The binding experiments were reproduced by two independent groups at the Department of Psychiatry, Columbia University (Dr. M. Quick) and at Division of Chemical Biology and Medicinal Chemistry, Eshelman School of Pharmacy, University of North Carolina at Chapel Hill (Dr. B. Roth). Replication of experiment details is found in each figure legend.

Statistics

All numerical results are reported as mean ± standard error of the mean (SEM). Data fits of binding isotherms were performed using nonlinear regression analysis in GraphPad Prism (RRID:SCR_002798), and the best-fit values and errors represent the mean and SEM of the fit. All numerical values used for graphs and detailed statistical analysis can be found in the figure legends as well as summarized in Table 1. Data assumed normal distribution, and so statistical significance of the difference between experimental groups was analyzed mainly with one-way ANOVA, two-way ANOVA, and unpaired *t* tests, depending on the number of groups and conditions, unless otherwise stated in the figure legend. Differences were considered statistically significant for $P \leq 0.05$ and denoted as *, $P \leq 0.05$; **, $P \leq 0.01$; ***, $P \leq 0.001$; ****, $P \leq 0.0001$.

Data Analysis Software

All statistical analyses were performed with GraphPad Prism 9 (RRID:SCR_002798) software. *In vivo* quantification of leukemia progression was performed with Living Image v4.7.2 (PerkinElmer, RRID:SCR_014247). Confocal images were analyzed using ImageJ (RRID:SCR_003070) software. Metabolomic data analysis was performed using Matplotlib for Python (RRID:SCR_008624). Flow cytometry data analysis was performed using FlowJo (RRID:SCR_008520) software. CRISPR-editing analysis was performed with the Synthego Performance Analysis (ICE Analysis, 2019, v2.0; Synthego). Biorender was used to create all the diagrams, cartoons, and schematics, under the Columbia University academic license. RNA-seq data analysis was done using the following software: STAR 2.7 (RRID:SCR_004463), featurecounts 1.6.5 (RRID:SCR_012919), R 3.6.3, Python 3.7.3 (IPython, RRID:SCR_001658), and GSEApy 0.9.18.

Data Availability

The RNA-seq data generated during this study are publicly available in GEO at GSE154374 (RRID: SCR_005012). Original/source data for Supplementary Fig. S3A are available at Protein Data Bank (#6E45; https://www.rcsb.org/structure/6E45). Derived data supporting the findings in Fig. 2I are shown in Supplementary Table S1. All other data supporting the findings of this study are available within the article and its Supplementary Data files.

Authors' Disclosures

M. Galán-Díez reports grants from Mandl Connective Tissue Research Fellowship during the conduct of the study. F. Borot reports other support from Vor Biopharma outside the submitted work; is a coinventor on issued patents and pending patent applications filed by Columbia University and exclusively licensed to Vor Biopharma and has received distributions of proceeds from the license granted by Columbia University to Vor Biopharma; and has been a consultant for Vor Biopharma. B.L. Roth reports grants from the NIH during the conduct of the study. S. Kousteni reports grants from the NIH/NIAMS, NIH/NHLBI, Edward P. Evans Foundation for MDS Research, and NIH/NCI during the conduct of the study. No disclosures were reported by the other authors.

Authors' Contributions

M. Galán-Díez: Conceptualization, data curation, formal analysis, funding acquisition, validation, investigation, visualization, methodology, writing–original draft, project administration, writing–review and editing. **F. Borot:** Resources, formal analysis, investigation, methodology. **A.M. Ali:** Resources, formal analysis, investigation. **J. Zhao:** Data curation, formal analysis. **E. Gil-Iturbe:** Formal analysis, investigation. **X. Shan:** Formal analysis, investigation. **N. Luo:** Investigation. **Y. Liu:** Investigation. **X. Huang:** Formal analysis. **B. Bisikirska:** Investigation. **R. Labella:** Investigation. **I. Kurland:** Resources, formal analysis. **B.L. Roth:** Resources. **M. Quick:** Resources, formal analysis, validation. **S. Mukherjee:** Resources. **R. Rabadan:** Resources. **M. Carroll:** Resources, validation, writing–review and editing. **A. Raza:** Resources. **S. Kousteni:** Conceptualization, resources, supervision, funding acquisition, validation, writing–original draft, project administration, writing–review and editing.

Acknowledgments

We thank Rene Hen, PhD, for the *Htr1b*$^{-/-}$ mice; P. Greengard, PhD, for *Htr1b*$^{fl/fl}$ mice; Roshan P. Shah, MD, for healthy patient samples; Mark Heany, MD, for AML samples; Yunping Qiu for technical assistance with metabolomic analysis; Michael P. Biagiotti for technical assistance with CRISPR/Cas9 assays; Israel S. Fernández, PhD, for metabolomic data analysis and critical discussion; and G. Karsenty, MD, PhD, and E. Passegué, PhD, for critical review and comments. We thank the Columbia Stem Cell Initiative Flow Cytometry core facility (directed by Michael Kissner). Funding for this research was provided by NIH AR054447, HL130937, the Edward P. Evans Foundation for MDS Research to S. Kousteni, and the Mandl Connective Tissue Research Fellowship awarded to M. Galán-Díez; NIH/NCI Cancer Center Support Grant P30CA013696 and the Stable Isotope and Metabolomics Core Facility of the Diabetes Research and Training Center (DRTC) of the Albert Einstein College of Medicine (NIH P60DK020541). The Oncology Precision Therapeutics and Imaging

Core (OPTIC) at the Herbert Irving Comprehensive Cancer Center at Columbia University shared resource was used.

The costs of publication of this article were defrayed in part by the payment of page charges. This article must therefore be hereby marked *advertisement* in accordance with 18 U.S.C. Section 1734 solely to indicate this fact.

Received May 27, 2021; revised November 8, 2021; accepted January 4, 2022; published first January 19, 2022.

REFERENCES

1. Zhang J, Niu C, Ye L, Huang H, He X, Tong W-G, et al. Identification of the haematopoietic stem cell niche and control of the niche size. Nature 2003;425:836–41.
2. Méndez-Ferrer S, Michurina TV, Ferraro F, Mazloom AR, Macarthur BD, Lira SA, et al. Mesenchymal and haematopoietic stem cells form a unique bone marrow niche. Nature 2010;466:829–34.
3. Méndez-Ferrer S, Bonnet D, Steensma DP, Hasserjian RP, Ghobrial IM, Gribben JG, et al. Bone marrow niches in haematological malignancies. Nat Rev Cancer 2020;127:2375–14.
4. Galán-Díez M, Cuesta-Domínguez Á, Kousteni S. The bone marrow microenvironment in health and myeloid malignancy. Cold Spring Harb Perspect Med 2018;8.
5. Yamashita M, Dellorusso PV, Olson OC, Passegué E. Dysregulated haematopoietic stem cell behaviour in myeloid leukaemogenesis. Nat Rev Cancer 2020;19:138–18.
6. Siegel RL, Miller KD, Jemal A. Cancer statistics, 2020. CA Cancer J Clin 2020;70:7–30.
7. Döhner H, Weisdorf DJ, Bloomfield CD. Acute myeloid leukemia. N Engl J Med 2015;373:1136–52.
8. Schepers K, Campbell TB, Passegué E. Normal and leukemic stem cell niches: insights and therapeutic opportunities. Stem Cell 2015;16:254–67.
9. Witkowski MT, Dolgalev I, Evensen NA, Ma C, Chambers T, Roberts KG, et al. Extensive remodeling of the immune microenvironment in B cell acute lymphoblastic leukemia. Cancer Cell 2020;37:867–82.
10. Raaijmakers MHGP, Mukherjee S, Guo S, Zhang S, Kobayashi T, Schoonmaker JA, et al. Bone progenitor dysfunction induces myelodysplasia and secondary leukaemia. Nature 2010;464:852–7.
11. Kode A, Manavalan JS, Mosialou I, Bhagat G, Rathinam CV, Luo N, et al. Leukaemogenesis induced by an activating β-catenin mutation in osteoblasts. Nature 2014;506:240–4.
12. Kode A, Mosialou I, Manavalan SJ, Rathinam CV, Friedman RA, Teruya-Feldstein J, et al. FoxO1-dependent induction of acute myeloid leukemia by osteoblasts in mice. Leukemia 2016;30:1–13.
13. Visnjic D, Kalajzic Z, Rowe DW, Katavic V, Lorenzo J, Aguila HL. Hematopoiesis is severely altered in mice with an induced osteoblast deficiency. Blood 2004;103:3258–64.
14. Bowers M, Zhang B, Ho Y, Agarwal P, Chen C-C, Bhatia R. Osteoblast ablation reduces normal long-term hematopoietic stem cell self-renewal but accelerates leukemia development. Blood 2015;125:2678–88.
15. Calvi LM, Adams GB, Weibrecht KW, Weber JM, Olson DP, Knight MC, et al. Osteoblastic cells regulate the haematopoietic stem cell niche. Nature 2003;425:836–41.
16. Dong L, Yu W-M, Zheng H, Loh ML, Bunting ST, Pauly M, et al. Leukaemogenic effects of Ptpn11 activating mutations in the stem cell microenvironment. Nature 2016;539:304–8.
17. Zambetti NA, Ping Z, Chen S, Kenswil KJG, Mylona MA, Sanders MA, et al. Mesenchymal inflammation drives genotoxic stress in hematopoietic stem cells and predicts disease evolution in human preleukemia. Cell Stem Cell 2016;19:613–27.
18. Frisch BJ, Ashton JM, Xing L, Becker MW, Jordan CT, Calvi LM. Functional inhibition of osteoblastic cells in an in vivo mouse model of myeloid leukemia. Blood 2012;119:540–50.
19. Krevvata M, Silva BC, Manavalan JS, Galán-Díez M, Kode A, Matthews BG, et al. Inhibition of leukemia cell engraftment and disease progression in mice by osteoblasts. Blood 2014;124:2834–46.
20. Wang W, Zimmerman G, Huang X, Yu S, Myers J, Wang Y, et al. Aberrant notch signaling in the bone marrow microenvironment of acute lymphoid leukemia suppresses osteoblast-mediated support of hematopoietic niche function. Cancer Res 2016;76:1641–52.
21. Medyouf H, Mossner M, Jann J-C, Nolte F, Raffel S, Herrmann C, et al. Myelodysplastic cells in patients reprogram mesenchymal stromal cells to establish a transplantable stem cell niche disease unit. Cell Stem Cell 2014;14:824–37.
22. Schepers K, Pietras EM, Reynaud D, Flach J, Binnewies M, Garg T, et al. Myeloproliferative neoplasia remodels the endosteal bone marrow niche into a self-reinforcing leukemic niche. Cell Stem Cell 2013;13:285–99.
23. Zhang B, Chu S, Agarwal P, Campbell VL, Hopcroft L, Jørgensen HG, et al. Inhibition of interleukin-1 signaling enhances elimination of tyrosine kinase inhibitor-treated CML stem cells. Blood 2016;128:2671–82.
24. Jilka RL, Weinstein RS, Bellido T, Roberson P, Parfitt AM, Manolagas SC. Increased bone formation by prevention of osteoblast apoptosis with parathyroid hormone. J Clin Invest 1999;104:439–46.
25. Haltalli MLR, Watcham S, Wilson NK, Eilers K, Lipien A, Ang H, et al. Manipulating niche composition limits damage to haematopoietic stem cells during Plasmodium infection. Nat Cell Biol 2020;505:1–12.
26. Corral J, Lavenir I, Impey H, Warren AJ, Forster A, Larson TA, et al. An Mll–AF9 fusion gene made by homologous recombination causes acute leukemia in chimeric mice: a method to create fusion oncogenes. Cell 1996;85:853–61.
27. Miller PG, Al-Shahrour F, Hartwell KA, Chu LP, Järås M, Puram RV, et al. In vivo RNAi screening identifies a leukemia-specific dependence on integrin beta 3 signaling. Cancer Cell 2013;24:45–58.
28. Krivtsov AV, Twomey D, Feng Z, Stubbs MC, Wang Y, Faber J, et al. Transformation from committed progenitor to leukaemia stem cell initiated by MLL-AF9. Nature 2006;442:818–22.
29. Yadav VK, Ryu J-H, Suda N, Tanaka KF, Gingrich JA, Schütz G, et al. Lrp5 controls bone formation by inhibiting serotonin synthesis in the duodenum. Cell 2008;135:825–37.
30. Saudou F, Amara DA, Dierich A, LeMeur M, Ramboz S, Segu L, et al. Enhanced aggressive behavior in mice lacking 5-HT1B receptor. Science 1994;265:1875–8.
31. Zhou BO, Yue R, Murphy MM, Peyer JG, Morrison SJ. Leptin-receptor-expressing mesenchymal stromal cells represent the main source of bone formed by adult bone marrow. Cell Stem Cell 2014;15:154–68.
32. DeFalco J, Tomishima M, Liu H, Zhao C, Cai X, Marth JD, et al. Virus-assisted mapping of neural inputs to a feeding center in the hypothalamus. Science 2001;291:2608–13.
33. Dacquin R, Starbuck M, Schinke T, Karsenty G. Mouse alpha1(I)-collagen promoter is the best known promoter to drive efficient Cre recombinase expression in osteoblast. Dev Cell 2002;224:245–51.
34. Zhang M, Xuan S, Bouxsein ML, Stechow von D, Akeno N, Faugere MC, et al. Osteoblast-specific knockout of the insulin-like growth factor (IGF) receptor gene reveals an essential role of IGF signaling in bone matrix mineralization. J Biol Chem 2002;277:44005–12.
35. Rodda SJ, McMahon AP. Distinct roles for Hedgehog and canonical Wnt signaling in specification, differentiation and maintenance of osteoblast progenitors. Development 2006;133:3231–44.
36. Mizoguchi T, Pinho S, Ahmed J, Kunisaki Y, Hanoun M, Mendelson A, et al. Osterix marks distinct waves of primitive and definitive stromal progenitors during bone marrow development. Dev Cell 2014;29:340–9.
37. Fontana F, Hickman-Brecks CL, Salazar VS, Revollo L, Abou-Ezzi G, Grimston SK, et al. N-cadherin regulation of bone growth and homeostasis is osteolineage stage-specific. J Bone Miner Res 2017;32:1332–42.
38. Gaster LM, Blaney FE, Davies S, Duckworth DM, Ham P, Jenkins S, et al. The selective 5-HT1B receptor inverse agonist 1′-methyl-5-[[2′-methyl-4“-(5-methyl-1,2, 4-oxadiazol-3-yl)biphenyl-4-yl]carbonyl]-2,3,6,7-tetrahydro- spiro[furo[2,3-f]indole-3,4-”piperidine] (SB-224289) potently blocks terminal 5-HT autoreceptor function both in vitro and in vivo. J Med Chem 1998;41:1218–35.
39. Percudani R, Peracchi A. A genomic overview of pyridoxal-phosphate-dependent enzymes. EMBO Rep 2003;4:850–4.

40. Chen C-C, Li B, Millman SE, Chen C, Li X, Morris JP, et al. Vitamin B6 addiction in acute myeloid leukemia. Cancer Cell 2020;37:771–77.
41. Djurec M, Graña O, Lee A, Troulé K, Espinet E, Cabras L, et al. Saa3 is a key mediator of the protumorigenic properties of cancer-associated fibroblasts in pancreatic tumors. Proc Natl Acad Sci 2018; 115:E1147–56.
42. Uhlar CM, Whitehead AS. Serum amyloid A, the major vertebrate acute-phase reactant. Eur J Biochem 1999;265:501–23.
43. Opitz CA, Litzenburger UM, Sahm F, Ott M, Tritschler I, Trump S, et al. An endogenous tumour-promoting ligand of the human aryl hydrocarbon receptor. Nature 2011;478:197–203.
44. Mulero-Navarro S, Fernandez-Salguero PM. New trends in aryl hydrocarbon receptor biology. Front Cell Dev Biol 2016;4:45.
45. Liu X, Shin N, Koblish HK, Yang G, Wang Q, Wang K, et al. Selective inhibition of IDO1 effectively regulates mediators of antitumor immunity. Blood 2010;115:3520–30.
46. Koblish HK, Hansbury MJ, Bowman KJ, Yang G, Neilan CL, Haley PJ, et al. Hydroxyamidine inhibitors of indoleamine-2,3-dioxygenase potently suppress systemic tryptophan catabolism and the growth of IDO-expressing tumors. Mol Cancer Ther 2010;9:489–98.
47. Yue EW, Sparks R, Polam P, Modi D, Douty B, Wayland B, et al. INCB24360 (epacadostat), a highly potent and selective indoleamine-2,3-dioxygenase 1 (IDO1) inhibitor for immuno-oncology. ACS Med Chem Lett 2017;8:486–91.
48. Farge T, Saland E, de Toni F, Aroua N, Hosseini M, Perry R, et al. Chemotherapy-resistant human acute myeloid leukemia cells are not enriched for leukemic stem cells but require oxidative metabolism. Cancer Discov 2017;7:716–35.
49. Duy C, Li M, Teater M, Meydan C, Garrett-Bakelman F, Lee T, et al. Chemotherapy induces senescence-like resilient cells capable of initiating AML recurrence. Cancer Discov 2021;11:1542–61.
50. Prendergast GC, Malachowski WP, DuHadaway JB, Muller AJ. Discovery of IDO1 inhibitors: from bench to bedside. Cancer Res 2017;77:6795–811.
51. Etxabe A, Lara-Castillo MC, Cornet-Masana JM, Banus-Mulet A, Nomdedeu M, Torrente MA, et al. Inhibition of serotonin receptor type 1 in acute myeloid leukemia impairs leukemia stem cell functionality: a promising novel therapeutic target. Leukemia 2017;31: 2288–302.
52. Banús-Mulet A, Etxabe A, Cornet-Masana JM, Torrente MÁ, Lara-Castillo MC, Palomo L, et al. Serotonin receptor type 1B constitutes a therapeutic target for MDS and CMML. Nat Cell Biol 2018;8:13883.
53. Ye H, Adane B, Khan N, Alexeev E, Nusbacher N, Minhajuddin M, et al. Subversion of systemic glucose metabolism as a mechanism to support the growth of leukemia cells. Cancer Cell 2018;34:659–73.
54. Fukuno K, Hara T, Tsurumi H, Shibata Y, Mabuchi R, Nakamura N, et al. Expression of indoleamine 2,3-dioxygenase in leukemic cells indicates an unfavorable prognosis in acute myeloid leukemia patients with intermediate-risk cytogenetics. Leuk Lymphoma 2015;56:1398–405.
55. Folgiero V, Goffredo BM, Filippini P, Masetti R, Bonanno G, Caruso R, et al. Indoleamine 2,3-dioxygenase 1 (IDO1) activity in leukemia blasts correlates with poor outcome in childhood acute myeloid leukemia. Oncotarget 2014;5:2052–64.
56. Chamuleau MED, van de Loosdrecht AA, Hess CJ, Janssen JJWM, Zevenbergen A, Delwel R, et al. High INDO (indoleamine 2,3-dioxygenase) mRNA level in blasts of acute myeloid leukemic patients predicts poor clinical outcome. Haematologica 2008;93:1894–8.
57. Mabuchi R, Hara T, Matsumoto T, Shibata Y, Nakamura N, Nakamura H, et al. High serum concentration of L-kynurenine predicts unfavorable outcomes in patients with acute myeloid leukemia. Leuk Lymphoma 2016;57:92–8.
58. Corm S, Berthon C, Imbenotte M, Biggio V, Lhermitte M, Dupont C, et al. Indoleamine 2,3-dioxygenase activity of acute myeloid leukemia cells can be measured from patients' sera by HPLC and is inducible by IFN-gamma. Leuk Res 2009;33:490–4.
59. Munn DH, Shafizadeh E, Attwood JT, Bondarev I, Pashine A, Mellor AL. Inhibition of T cell proliferation by macrophage tryptophan catabolism. J Exp Med 1999;189:1363–72.
60. Munn DH, Mellor AL. Indoleamine 2,3-dioxygenase and tumor-induced tolerance. J Clin Invest 2007;117:1147–54.
61. Chung DJ, Rossi M, Romano E, Ghith J, Yuan J, Munn DH, et al. Indoleamine 2,3-dioxygenase-expressing mature human monocyte-derived dendritic cells expand potent autologous regulatory T cells. Blood 2009;114:555–63.
62. Hwu P, Du MX, Lapointe R, Do M, Taylor MW, Young HA. Indoleamine 2,3-dioxygenase production by human dendritic cells results in the inhibition of T cell proliferation. J Immunol 2000;164:3596–9.
63. Munn DH, Sharma MD, Baban B, Harding HP, Zhang Y, Ron D, et al. GCN2 kinase in T cells mediates proliferative arrest and anergy induction in response to indoleamine 2,3-dioxygenase. Immunity 2005;22:633–42.
64. Lemos H, Huang L, Prendergast GC, Mellor AL. Immune control by amino acid catabolism during tumorigenesis and therapy. Nat Rev Cancer 2019;19:162–75.
65. Platten M, Nollen EAA, Röhrig UF, Fallarino F, Opitz CA. Tryptophan metabolism as a common therapeutic target in cancer, neurodegeneration and beyond. Nat Rev Drug Discov 2019;18:379–401.
66. Long GV, Dummer R, Hamid O, Gajewski TF, Caglevic C, Dalle S, et al. Epacadostat plus pembrolizumab versus placebo plus pembrolizumab in patients with unresectable or metastatic melanoma (ECHO-301/KEYNOTE-252): a phase 3, randomised, double-blind study. Lancet Oncol 2019;20:1083–97.
67. Komrokji RS, Wei S, Mailloux AW, Zhang L, Padron E, Sallman D, et al. A phase II study to determine the safety and efficacy of the oral inhibitor of indoleamine 2,3-dioxygenase (IDO) enzyme INCB024360 in patients with myelodysplastic syndromes. Clin Lymphoma Myeloma Leuk 2019;19:157–61.
68. Yates JW, Wallace HJ, Ellison RR, Holland JF. Cytosine arabinoside (NSC-63878) and daunorubicin (NSC-83142) therapy in acute nonlymphocytic leukemia. Cancer Chemother Rep 1973;57:485–8.
69. Döhner H, Estey E, Grimwade D, Amadori S, Appelbaum FR, Büchner T, et al. Diagnosis and management of AML in adults: 2017 ELN recommendations from an international expert panel. Blood 2017;129:424–47.
70. Abraham M, Klein S, Bulvik B, Wald H, Weiss ID, Olam D, et al. The CXCR4 inhibitor BL-8040 induces the apoptosis of AML blasts by downregulating ERK, BCL-2, MCL-1 and cyclin-D1 via altered miR-15a/16-1 expression. Leukemia 2017;31:2336–46.
71. Natoni A, Smith TAG, Keane N, McEllistrim C, Connolly C, Jha A, et al. E-selectin ligands recognised by HECA452 induce drug resistance in myeloma, which is overcome by the E-selectin antagonist, GMI-1271. Leukemia 2017;31:2642–51.
72. Ben-Batalla I, Schultze A, Wroblewski M, Erdmann R, Heuser M, Waizenegger JS, et al. Axl, a prognostic and therapeutic target in acute myeloid leukemia mediates paracrine crosstalk of leukemia cells with bone marrow stroma. Blood 2013;122:2443–52.
73. Waizenegger JS, Ben-Batalla I, Weinhold N, Meissner T, Wroblewski M, Janning M, et al. Role of growth arrest-specific gene 6-Mer axis in multiple myeloma. Leukemia 2015;29:696–704.
74. Virk MS, Sagi Y, Medrihan L, Leung J, Kaplitt MG, Greengard P. Opposing roles for serotonin in cholinergic neurons of the ventral and dorsal striatum. Proc Natl Acad Sci 2016;113:734–9.
75. Rached M-T, Kode A, Xu L, Yoshikawa Y, Paik J-H, DePinho RA, et al. FoxO1 Is a positive regulator of bone formation by favoring protein synthesis and resistance to oxidative stress in osteoblasts. Cell Metab 2010;11:147–60.
76. Patel N, Huang X-P, Grandner JM, Johansson LC, Stauch B, McCorvy JD, et al. Structure-based discovery of potent and selective melatonin receptor agonists. Elife 2020;9:e53779.
77. Dobin A, Davis CA, Schlesinger F, Drenkow J, Zaleski C, Jha S, et al. STAR: ultrafast universal RNA-seq aligner. Bioinformatics 2013;29: 15–21.
78. Liao Y, Smyth GK, Shi W. featureCounts: an efficient general purpose program for assigning sequence reads to genomic features. Bioinformatics 2014;30:923–30.
79. Love MI, Huber W, Anders S. Moderated estimation of fold change and dispersion for RNA-seq data with DESeq2. Genome Biol 2014;15:550.